RESEARCH

High-grade metamorphism of banded iron formations: the role of saline fluids in promoting the growth of pyroxene and garnet reaction textures along magnetite-quartz grain boundaries

Paul M. George[1,2,3] · Daniel E. Harlov[4,5,6] · Brian F. Windley[7] · Madhusoodhan Satish-Kumar[8] · Krishnan Sajeev[3] · Ming-Guo Zhai[5,9]

Abstract

Metamorphosed banded iron formation (BIF) in granulite-amphibolite facies, tonalitic orthogneisses from a series of locations in the Kolli Massif of southern India are described and analysed with regard to their lithologies, whole rock chemistry, mineral reaction textures, and mineral chemistry. On the basis of their mineral reaction textures along magnetite-quartz grain boundaries these BIFs are grouped according to their predominant silicate mineralogy: 1) amphibole; 2) orthopyroxene; 3) orthopyroxene–clinopyroxene; 4) orthopyroxene-clinopyroxene-garnet; 5) clinopyroxene-garnet-plagioclase; and 6) Fe-Mg silicates are absent. Two-pyroxene and garnet-pyroxene Fe-Mg exchange thermometry, coupled with thermodynamic pseudosection modelling of whole rock data from one of the magnetite-quartz-orthopyroxene-clinopyroxene-bearing lithologies, indicates that the magnetite-quartz-orthopyroxene-clinopyroxene-garnet assemblages formed at ~900 to 1200 MPa and 750 to 900 °C under relatively low H_2O activities. Magnetite-quartz-orthopyroxene reaction textures were experimentally replicated at 800 and 900 °C and 1000 MPa in a synthetic BIF using isolated magnetite grains in a quartz matrix to which was added a hypersaline Mg- and Al-bearing fluid (approximately 1% by mass), which permeated along all the grain boundaries. The fact that Fe-Mg silicate reaction textures did not form in one of the BIF samples, which had experienced the same $P\text{-}T$ conditions as the other BIF samples, suggests that, unless a BIF initially incorporated Mg, Al, and Ca during formation with or was infiltrated from the surrounding rocks by Mg-, Al-, and Ca-bearing saline fluids, these silicate minerals could not and would not have formed from the inherent magnetite and quartz during granulite-facies and amphibolite-facies metamorphism.

Keywords Magnetite · Orthopyroxene · Clinopyroxene · Banded iron formations (BIFs) · Kolli Massif · Southern India

Introduction

Banded iron formations (BIFs) are traditionally considered to have originated as marine chemical sediments consisting of alternating bands of Fe oxides and amorphous silica that

were deposited in deep still waters during anoxic Archean and Paleoproterozoic eras of Earth history (Bekker et al. 2010, 2014). As a consequence, they have a long geological history during which these rocks were modified by varying degrees of tectonic activity and metamorphism ranging from low-grade (e.g., Johnson et al. 2003; Rasmussen et al. 2014,

✉ Daniel E. Harlov
  dharlov@gfz-potsdam.de

1 School of Mining and Geosciences, Nazarbayev University, Astana 010000, Kazakhstan

2 State Key Laboratory for Continental Dynamics, Department of Geology, Northwest University, Xian 710069, China

3 Centre for Earth Sciences, Indian Institute of Science, Bangalore 560012, India

4 Deutsches GeoForschungsZentrum GFZ, Telegrafenberg, Potsdam 14473, Germany

5 Faculty of Earth Resources, China University of Geosciences, Wuhan 430074, China

6 Department of Geology, University of Johannesburg, Auckland Park 2006, South Africa

7 School of Geology, Geology and the Environment, The University of Leicester, Leicester LE1 7RH, UK

8 Department of Geology, Niigata University, 2-8050 Ikarashi, Nishi-ku, Niigata 950-2181, Japan

9 Institute of Geology and Geophysics, Chinese Academy of Sciences, Beijing 100 069, China

2016, 2017; Mloszewska et al. 2012) to high-grade (Klein 1978, 2005; Prasad et al. 1982; Zhai and Windley 1990; Zhai et al. 1990). BIFs are present in all the major cratons of the world where they serve as one of the principal repositories for iron ore (Table 1). During the past few decades, they have been widely investigated particularly with regard to understanding the evolution of the early Earth's atmosphere and ocean water chemistry along with the episodic rise of oxygen (Holland 2006; Ohmoto et al. 2006; Frei and Polat 2007; Frei et al. 2008; Bekker et al. 2010; Kasting 2013; Lyons et al. 2014; Konhauser et al. 2017).

High-grade, metamorphosed BIFs (amphibolite-granulite-eclogite facies) are generally characterized by the presence of silicate minerals, such as orthopyroxene, clinopyroxene, olivine, garnet, and/or amphibole along with ubiquitous quartz, magnetite and/or hematite (Table 1). Minor minerals can include plagioclase, graphite (French 1968; Butler 1969), pyrite (Butler 1969), pyrrhotite (French 1968; Klein 1978), and biotite/phlogopite (Klein 1978; Lan et al. 2019b). While a few high-grade BIF are situated in what could be called a contact metamorphic aureole, most high-grade BIFs in the world are located in orogenic belts, or in lower crustal gneissic cratons where they mostly occur as enclaves, lenses, and layers in belts of schist, amphibolite, or granulite-facies gneiss (e.g. Klein 1978, 2005; Sandiford and Powell 1986; Harley 1987; Zhai et al. 1990). The general petrography and *P-T* conditions of several of these high-grade BIF have been well documented; however little is known about the specific crustal processes that were responsible for or facilitated their formation, or about their links to the evolution of their respective terrains.

The aim of this paper is to report the results of a study of mineral assemblages from a series of high-grade BIFs

associated with amphibolite-, granulite-, and eclogite-grade lithologies in the Kolli Massif in southern India (Fig. 1) (Saravanan 1969; Prasad et al. 1982; Thirunavukkarasu et al. 2015; George and Sajeev 2015; Yellappa et al. 2016). We present a detailed mineralogical, petrological, and geochemical analysis of the varied BIF lithologies along with a general estimation of the *P-T* conditions during their formation. Orthopyroxene reaction textures observed along magnetite-quartz grain boundaries are then replicated by an experimental study under similar *P-T* conditions experienced by the natural BIFs during high grade metamorphism by utilizing saline to hypersaline Mg- and Al-bearing fluids. These two lines of investigation are combined to explain the role of element mass transfer in high-grade BIF lithologies during their physical transport down and then up a presumed subduction-exhumation channel to and from the deep crust or lithospheric mantle.

Geological setting and background

The Archean Dharwar Craton makes up a large segment of central and southern India (Fig. 1). It is composed of a mosaic of crustal blocks of variable ages mutually separated by deep crustal shear/suture zones (e.g., Jayananda et al. 2006, 2015, 2018, 2020, 2023; Ratheesh-Kumar et al. 2020). The Dharwar Craton mainly consists of tonalitic-trondhjemitic-granodioritic (TTG) gneisses, volcano-sedimentary greenstone belts, and several large potassic and calc-alkaline granitic intrusions that are mostly Neoarchean in age (Fig. 1; Gireesh et al. 2012; Tushipokla 2013; Mohan et al. 2014). These include greenschist-grade schist belts and granitic intrusions along with sinistral shear zones that

Table 1 Major metamorphosed BIFs worldwide

Location	Assemblage	Age (Ga)	References
Hamersely Basin, Yilgarn Block, Western Australia	Mag-Qz-Opx-Ol-Grunerite	2.7–2.6	Gole and Klein (1981)
Biwabik Iron Formation, Minnesota, USA; Gunflint, Ontario, Canada	Mag-Qz-Ol	1.85	Bonnichsen (1969), Morey et al. (1972), Simmons et al. (1974), Floran and Papike (1978), Klein (1983)
Fyfe Hills, Enderby Land, Antarctica	Mag-Qz-Opx	2.6	Sandiford and Powell (1986)
Napier Complex, Tonagh Island, Enderby Land, Antarctica	Mt-Qtz-Opx	2.6	Sandiford and Powell (1986), Harley (1987)
Wind River Range, Wyoming, USA	Mag-Qz-Opx-Grt	2.7–2.5	Immega and Klein (1976), Vaniman et al. (1980), Sharp et al. (1988)
North China Craton, NE China	Mag-Qz-Opx	2.86–2.83	Zhai and Windley (1990), Zhai et al. (1990)
Vornezeh Crystalline Massif, Russia	Mag-Qz-Opx-Cpx-Pl	3.178	Fonarev et al. (2006)
Bhandara-Balaghat granulite, Sauser Mobile Belt, Central Indian Tectonic Zone, India	Mag-Qz-Opx-Cpx±Grt	1.5	Bhowmik et al. (2006)
Southern margin of North China Craton, China	Mag-Qz-Opx-Cpx±Amp±Grt±Bt	2.5,1.8	Lan et al. (2019a,b), Huang et al. (2019)

Mt magnetite, *Qtz* quartz, *Opx* orthopyroxene, *Cpx* clinopyroxene, *Ol* olivine, *Grt* garnet, *Pl* plagioclase, *Amh* amphibole
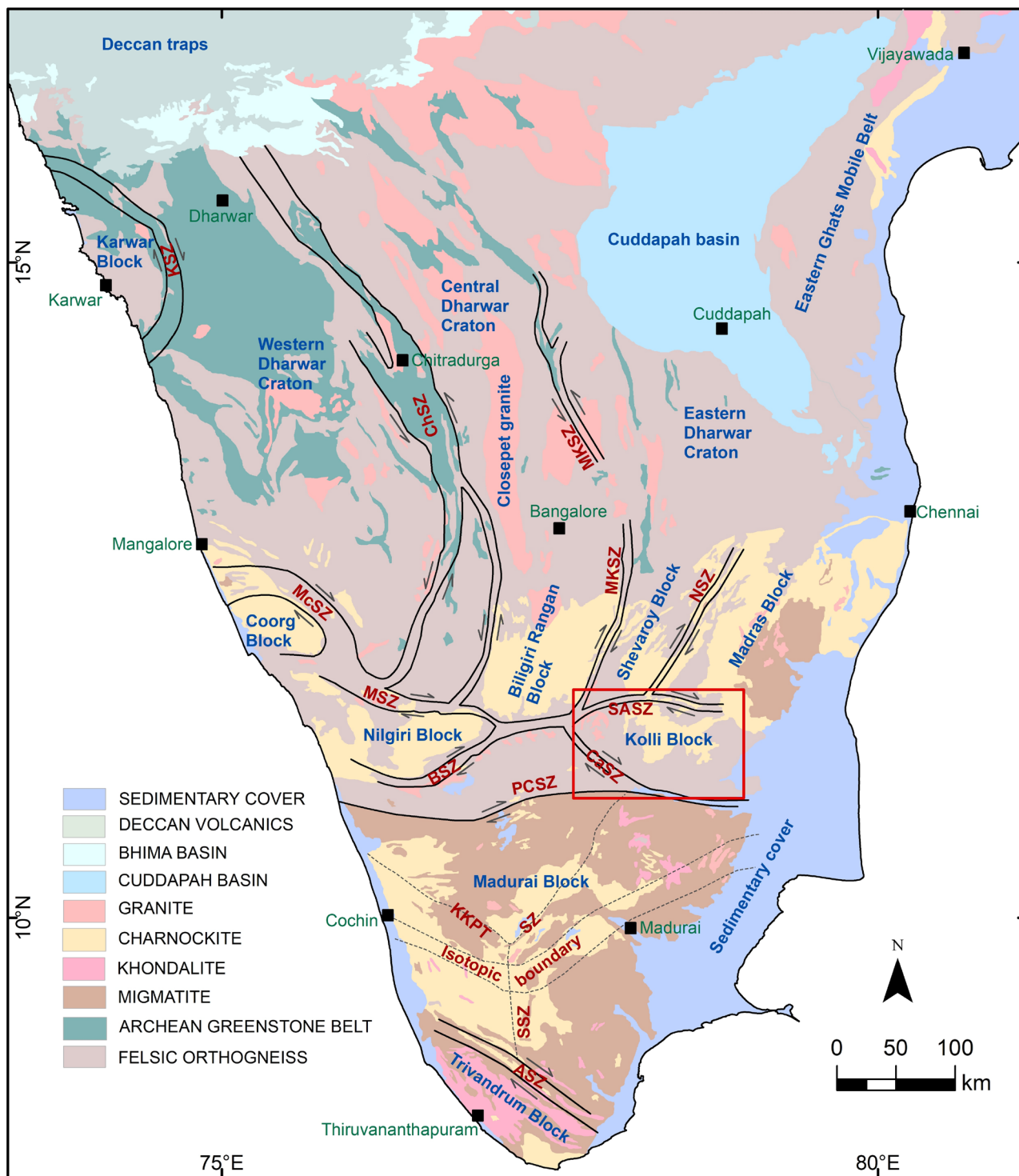
Fig. 1 Regional geology and tectonic framework of southern India (Geological Survey of India 1995; Drury and Holt 1980; Ishwar-Kumar et al. 2013). A box outlines the Kolli Block (Kolli massif). Acronyms: KSZ- Kumta shear zone, McSZ- Mercara shear zone, ChSZ- Chitradurga shear zone, SaSZ- Sargur Shear Zone, KoSZ-Kollegal Shear Zone, MKSZ- Mettur-Kolar shear zone, NSZ-Nallamalai shear zone, MSZ- Moyar shear zone, SASZ- Salem-Attur shear zone; BSZ- Bhavani shear zone, CaSZ- Cauvery shear zone, PCSZ- Palghat-Cauvery shear zone; KKPTSZ- Karur-Kambam-Painavu-Trichur shear zone, ASZ- Achankovil shear zone)

were formed by late Archean NE-SW crustal shortening (Chadwick et al. 2000; Ishwar-Kumar et al. 2013). The southern part is characterised by predominantly N-S to NE-SW structural trends (Chardon et al. 2008; Peucat et al. 2013) and is bound by amphibolite- to orthopyroxene-bearing granulite-grade gneisses along its southern margin (Ghosh et al. 2004; Ratheesh-Kumar et al. 2020).

The Dharwar Craton is divided into Western, Central, and Eastern Cratons (Jayananda et al. 2018; Ratheesh-Kumar et al. 2020) (Fig. 1). The Western and Central Cratons are separated by the Chitradurga schist belt (e.g., Hokada et al. 2013; Lancaster et al. 2014; Sreehari and Toyoshima 2020), and the Central and Eastern Cratons by the Kolar suture zone (Jayananada et al. 2013; Yang and Santosh 2015). Published geochronological results and Nd model ages indicate a magmatic age range for the Western Dharwar Craton of 3400 to 2900 Ma (e.g., Jayananda et al. 2000, 2015, 2018, 2023; Dey 2013; Mohan et al. 2014; Maibam et al. 2016); a magmatic age range of 3400 to 2500 Ma for the Central Dharwar Craton (e.g., Peucat et al. 2013; Ratheesh-Kumar et al. 2016); and a magmatic age range of mostly between 2700 and 2500 Ma for the Eastern Dharwar Craton (Clark et al. 2009; Gireesh et al. 2012; Glorie et al. 2014; Manikyamba et al. 2015; Hazarika et al. 2015; Maibam et al. 2016; Jayananda et al. 2020).

The southern margin of the Dharwar Craton is divided by ductile shear zones into a set of tectonic blocks of granulite grade (Chardon et al. 2008), which are dominated by orthopyroxene-bearing TTG gneisses, and mutually separated by shear/suture zones (Fig. 1; Ghosh et al. 2004; Chardon et al. 2008; Peucat et al. 2013; Ishwar-Kumar et al. 2013; Collins et al. 2014; Ratheesh-Kumar et al. 2016, 2020). They are sometimes given other names or several of these blocks are grouped into one block (e.g. the Salem Block of Glorie et al. (2014) which consists of the Shevaroy, Kolli, and Madras Blocks in Fig. 1). In Fig. 1, following Ishwar-Kumar et al. (2013) these blocks are termed the Coorg Block (Chetty et al. 2012; Ishwar-Kumar et al. 2013, 2016; Santosh et al. 2015); the Nilgiri Block (Samuel et al. 2014, 2019), the Biligiri Rangan Block (Peucat et al. 2013; Ratheesh-Kumar et al. 2016); the Shevaroy Block (Li et al. 2018; Harlov et al. 2022); the Kolli Block (named after the Kolli Massif but also known as the Namakkal Block) (George and Sajeev 2015; Behera et al. 2019; Gou et al. 2022); and the Madras Block (Rameshwar Rao et al. 1991a, b; Braun and Kriegsman 2003). These granulite facies blocks, which extend from west to east across southern India (Fig. 1), are separated from the Madurai Block to the south by the Palghat-Cauvery shear zone (Plavsa et al. 2012, 2014; Peucat et al. 2013; Santosh et al. 2009).

The Kolli Block

The Kolli Block consists primarily of the Kolli Massif (Fig. 1). It is bounded by the E-W-trending Salem Attur Shear Zone that separates it from the Shevaroy and Madras Blocks to the north, and by the Cauvery Shear Zone, which separates it from the Madurai Block to the south (Figs. 1 and 2). The Kolli Massif consists of orthopyroxene-bearing granulite facies gneisses, amphibolite-facies TTG gneisses, magnetite quartzites (BIFs), marbles, and layered igneous complexes (calcic anorthosite, leucogabbro, gabbro, eclogite, garnet websterite, and two-pyroxene granulite) (Fig. 2; Bhaskar Rao et al. 1996; Ghosh et al. 2004; Ram-Mohan et al. 2013; George et al. 2019; He et al. 2021; Gou et al. 2022).

To the west of the Kolli Massif at Sankagiri (also Sankaridrug) (Fig. 2) diopside-hornblende gneisses occur within a *ca*. 250 m-wide belt of marbles that extends along strike for about 32 km. The whole package is intruded by younger granites (Fig. 2). These pure calcite (limestone) marbles, contain 30 cm-wide layers of garnet-diopside and garnet-epidote, but no evidence of internal thrusts, isoclinal folds, or duplicated stratigraphy. We assume such a thick carbonate sequence was most probably derived from a carbonate shelf on a passive continental margin.

The BIFs occur as layers conformable with the surrounding country rock, which include TTG gneisses and orthopyroxene-bearing charnockitic gneisses. They can range up to a few meters wide and several kilometres long (Fig. 2). The BIF are internally foliated, sheared, and folded, and become more deformed and recrystallised in the vicinity of the boundary shear zones (see Fig. 3b). At Kanjamalai layers of BIF are folded into a spectacular interference pattern (Fig. 2). Eleven BIF localities were sampled across the Kolli Massif (Table 2; Fig. 2). Polished thin sections were made of these samples using normal routine methods. The thin sections from these samples were then characterized with respect to their mineralogy and petrography using transmitted and reflected light petrographic microscopy. The samples were also analysed with respect to their whole-rock chemistry. The field relations and description of these samples are given below.

BIF field relations and sample descriptions

BIF-1 was collected from the crest of a hillock to the NE of Salem city (N11.6869, E78.3132), which is within the Salem Attur Suture/Shear Zone (Fig. 2). The BIF is weakly banded/foliated (Fig. 3a) or mylonitized and sheared (Fig. 3b).

BIF-2 was sampled to the southeast of Salem (N11.6265, E78.3360; Fig. 2) where it is intercalated with a garnetiferous gabbro and a pyroxene granulite. **BIF-11** (Fig. 3l)
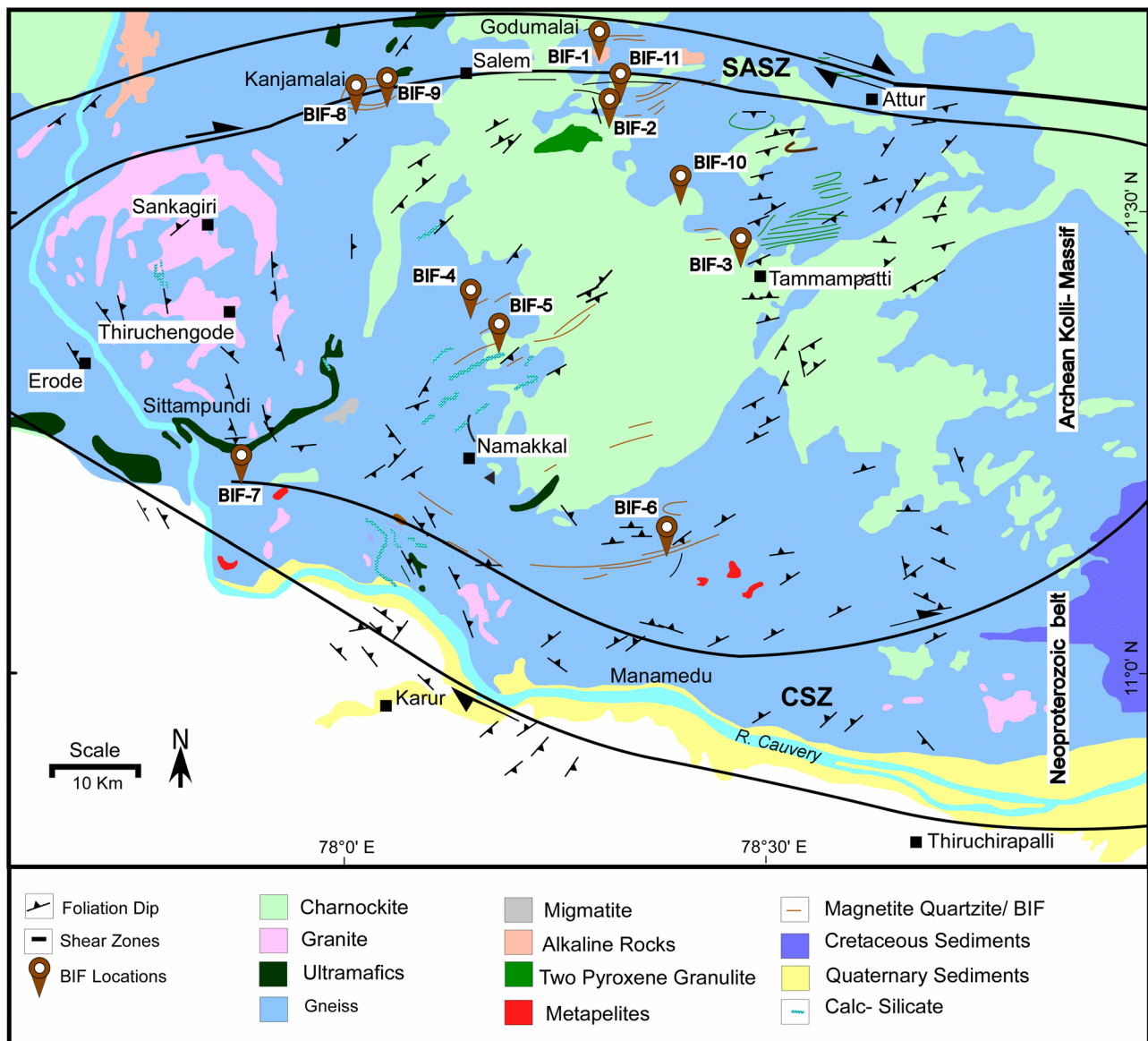
Fig. 2 Geological map of the Kolli Massif (modified after George and Sajeev 2015; George et al. 2019) showing BIF sample locations and towns mentioned in this study

was collected about 200 m away from **BIF-2** at N11.6266, E78.3361 (Fig. 2), and has similar lithological relations. Samples from both localities are massive and are not banded (compare Fig. 3a, b with l).

In the poorly exposed eastern Kolli Massif (Fig. 2), the BIFs occur mostly as boulders. **BIF-3** is from a rare massive outcrop without banding (N11.4598, E78.4951) (Fig. 3d). Quartzite and garnetiferous massive orthopyroxene-bearing charnockitic granite are close by, but their field relationships are unclear.

Directly south of Salem, near the Salem-Namakkal highway, there are EW-trending metamorphosed massive BIF (Fig. 3e) in meter-long, rarely banded, layers about 3 m wide, which are bordered by garnet- and orthopyroxene-bearing

charnockitic gneiss and two-pyroxene granulite (N11.3941, E78.1744) (Fig. 2). **BIF-4** was sampled on the northern side (N11.3628, E78.1838) of a 19 km long BIF layer that continues into the orthopyroxene-gneiss area (Fig. 2).

BIF-5, which is from an outcrop in a paddy field at a village near Namakkal away from the Salem-Namakkal highway, is very coarse-grained and has no banding (Fig. 2). The Fe oxide minerals appear to be segregated (Fig. 3f) possibly due to recrystallization during metamorphism. The BIF locality is surrounded by granitic gneiss, whose relationship with the BIF outcrop is obscure.

BIF-6 was sampled from a metamorphosed BIF close to a garnetiferous meta-gabbro in the southern margin of

Fig. 3 Field photographs of various field exposures of the granulite-grade BIF in the Kolli Massif: **a**, **b BIF-1**, **c BIF-2**, **d BIF-3**, **e BIF-4**, **f BIF-5**, **g BIF-6**, **h BIF-7**, **i BIF-8**, **j BIF-9**, **k BIF-10**, and **l BIF-11** (see also Table 2)

Table 2 BIF mineral abundances

Sample	longitude	latitude	Mag	Qz	Opx	Cpx	Grt	Amp	Bt	Pl	Kfs
BIF-1	11.6869	78.3132	x	x				x			
BIF-2	11.6265	78.336	x	x	x	x					
BIF-3	11.4598	78.4951	x	x	x	x					
BIF-4	11.3941	78.1744	x	x	x						
BIF-5	11.3628	78.1838	x	x	x	Augite					
BIF-6	11.1313	78.4174	x	x	x	x	x				
BIF-7	11.2145	77.8813	x	x							
BIF-8	11.6294	78.0526	x	x	x			x			
BIF-9	11.6095	78.0371	x	x	x			x			
BIF-10	11.5366	78.422	x	x	x				x		
BIF-11	11.6266	78.3361	x	x	x	x	x			x	x

Mag magnetite, *Qz* quartz, *Opx* orthopyroxene, *Cpx* clinopyroxene, *Grt* garnet, *Amp* amphibole, *Bt* biotite, *Pl* plagioclase, *Kfs* K-feldspar, *Blank* mineral is absent

the Kolli Massif near the Cauvery Shear Zone (Fig. 2). The BIF is associated with garnetiferous meta-gabbro, garnet-pyroxenite, amphibolite, and two pyroxene granulite. Yellappa et al. (2012) reported a U-Pb zircon age of ca. 2528 Ma from a nearby trondhjemite 2 kms east of the BIF-6 sample site. Chowdhury and Chakraborty (2019) determined that the peak metamorphic conditions of a metagabbro (2 kms north of the BIF location) associated with a BIF were 800 °C and 1200 to 1400 MPa, followed by cooling and decompression at 710 °C and 1000 to 1100 MPa to 580 to 600 to 800 MPa at 620 °C. George et al. (2019) estimated peak metamorphic conditions of 980 °C and 2200 MPa for a 2526 Ma garnet-bearing pyroxenite (south of this locality). Weakly banded **BIF-6** was collected at N11.1313, E78.4174 from a rock pile at a well cutting (Fig. 3g).

To the southwest of the Kolli Massif thin layers of metamorphosed BIF are situated along the margin of and within the Sittampundi Complex, which consists of layered chromite-bearing anorthosite, leucogabbro, meta-gabbro, amphibolite, and websterite (Fig. 2). Subramaniam (1956) reported eclogitic garnet-clinopyroxene rocks within the Complex. In a layered leucogabbro, Sajeev et al. (2009) described 30-cm lenses of omphacite-bearing eclogite (Na_2O wt.% > 4) that had an estimated temperature and pressure of 1020 °C and 2000 MPa. From the Sittampundi Complex, Bhaskar Rao et al. (1996) estimated a ca. 2900 Ma Sm-Nd whole-rock isochron age for a meta-gabbro, and a ca. 730 Ma age for a garnet-bearing granulite based on a garnet-plagioclase-hornblende Sm-Nd isochron. Ram-Mohan et al. (2013) reported that an associated anorthosite has a zircon U-Pb age of ca. 2541 Ma and that zircon Hf isotopes have positive εHf values, ($εHf = ((^{176}Hf/^{177}Hf)_{Sample} - ^{176}Hf/^{177}Hf)_{Chon}/ ^{176}Hf/^{177}Hf)_{Chon})) \times 10000$), indicating the magma source was juvenile. From the chromite-silicate chemistry, Dharma Rao et al. (2013) concluded that the Sittampundi Complex was generated in a subduction-related arc. He

et al. (2021) suggested that the Sittampundi anorthosite had a minimum emplacement age of ca. 2526 Ma (U-Pb zircon), and that zircons in the anorthosite have a 'mantle like' $δ^{18}O$ composition. Within the Sittampundi Complex, **BIF-7** was sampled from a metamorphosed, weakly banded BIF layer (N11. 2145, E77.8813), which was in direct contact with a meta-gabbro (Figs. 2 and 3h).

At Kanjamalai, west of Salem city (Fig. 2), a 3 to 6 km-wide refolded isoclinal synform contains layers, up to ca. 20 to 40 m wide, of granulite-facies BIF intercalated with websterites, partly amphibolitised meta-gabbros, two-pyroxene granulites, and granitic sheets (Saravanan 1969). Sato et al. (2011) reported that zircons in the granitic sheets have an age of 2.65 Ga. Noack et al. (2013) dated the peak of metamorphism at 2480 Ma for a garnetiferous mafic granulite using Lu-Hf garnet dating. This suggests that crustal formation was in the Archean, and subsequent metamorphism was in the Paleoproterozoic (Anderson et al. 2012). Mukhopadhayay and Bose (1994) first identified granulite- to eclogite-facies metamorphism in the Kanjamalai meta-gabbros (garnet + clinopyroxene +/- orthopyroxene +/- plagioclase + hornblende +/- Fe-Ni oxides). Anderson et al. (2012) reported *P-T* conditions at ca. 1400 to 1600 MPa and 820 to 860 °C with an age of ca. 2490 Ma. Saitoh et al. (2011) reported that peak high-pressure metamorphism was lower at 800 to 1200 MPa and 750 to 800 °C. In one of the few structural investigations of the region, Mohanty and Chetty (2014) described a thrust-controlled detachment in a mélange with sheath folds near the margin of the Kanjamalai rocks. The BIF samples collected from the Sittampundi Complex are **BIF-8** (N11.6294, E78.05226; Fig. 3i), which is associated with a garnet-bearing meta-gabbro and pyroxene granulite, and **BIF-9** (N11.6095, E78.0371; Fig. 3j), which is bordered by a websterite.

BIF-10 (Fig. 3k) was collected from metamorphosed BIF layers east of Salem (N11.5366, E78.422) (Fig. 2), which

are intercalated with granitic gneiss, quartzite, and pyroxene granulite, whose mutual geological relationships are unclear.

Methods

Whole-rock chemistry

Major element concentrations were measured for the 11 BIF samples by X-ray fluorescence (XRF) spectrometry using a Rigaku RIX 3000 system at the Department of Geology, Niigata University, Niigata, Japan (Table 3). Initial sample size was 2 kg. Glass disks were prepared by fusing a rock powder sample (0.5 g) with Li tetraborate ($Li_2B_4O_7$, 5.0 g) for major element analyses. The full analytical procedure is described by Takahashi and Shuto (1997), and more recently by Flude et al. (2017).

Electron microprobe (EMP) analyses

The mineral chemistry of the magnetite (Table 4; Supplementary Appendix 1a), pyroxenes (Table 5; Supplementary Appendix 1b), and garnet (Table 6; Supplementary Appendix 1c) were determined with a JEOL JXA-8230 Electron Microprobe (EMP) housed in the Advanced Facility for Microscopy and Microanalysis (AFMM) at the Indian Institute of Science, Bangalore, India; a JEOL JXA-8900 EMP in Okayama University of Science, Okayama, Japan; and a JEOL JXA-8230 EMP at the State Key laboratory of Continental Dynamics, Department of Geology, Northwest University, Xian, China. Carbon coating on all of the thin sections analysed was 20 nm.

Analytical conditions were identical in the facilities from India and Japan; during the analyses, the acceleration voltage during the analysis was 15 kV, the beam current was 12 nA, and the beam diameter was 3 microns. For analyses at

Northwest University the accelerating voltage was 15 kV, the beam current was 20 nA, and the beam diameter size was 2 microns. Matrix corrections were performed using software supplied by JEOL, i.e. the data were reduced using standard ZAF correction procedures. In order to ensure that the relative differences observed are correct within EMP error, all analyses per sample were obtained during one single measuring session including multiple checks of the calibration.

In general, anywhere from 4 to 5 silicate and oxide grains, scattered evenly over the length and breadth of the thin section, were analysed per sample. Five to ten EMP analysis points were generally taken per mineral grain. Unless otherwise specified, only mineral cores were analysed and rims avoided. This was done in order to obtain compositions, which are as close as possible to the peak metamorphic conditions present during the granulite-facies metamorphism of the BIF samples. For each of the three EMP, the standards used for analysis of the magnetite and silicate minerals were Ca-Diopside; Ti-Rutile; Na-Jadeite; Al-Almandine; Mg-Olivine; Si-quartz; Fe-Magnetite; Mn-Rhodonite; V – V metal, and Cr- Chromium oxide.

Experimental procedure and analytical technique

In order to reproduce the subsequent silicate reaction textures growing along magnetite-quartz grain boundaries under the high-grade conditions experienced by the BIFs, experiments were constructed that involved natural grains of magnetite (50–500 μm) surrounded by a synthetic quartz matrix (Table 7). To this was added about 1 mg of doubly distilled pure H_2O or 1 M $MgCl_2$ solution to act as a flux along with variable small amounts of $MgCl_2$, MgO, anorthite glass, and/or Al_2O_3 (Table 7). Magnesium and Al were added to the system because the stability of orthopyroxene at high *P-T* is a function of the Mg and Al content of the orthopyroxene as well as the pressure, temperature, and H_2O

Table 3 Whole rock major element chemistry

Sample No	BIF-1	BIF-2	BIF-3	BIF-4	BIF-5	BIF-6	BIF-7	BIF-8	BIF-9	BIF-10	BIF-11
P_2O_5	0.22	0.15	0.42	0.04	0.28	0.34	0.15	0.09	0.51	0.18	0.09
SiO_2	44.5	54.3	47.5	60.9	48.6	47.6	51.0	48.6	51.0	50.3	78.2
TiO_2	bdl	0.02	bdl	0.01	bdl	0.22	0.01	0.01	0.01	bdl	0.04
Al_2O_3	0.46	1.08	0.49	0.54	0.44	1.73	0.56	0	0.45	0.44	1.44
MgO	1.25	2.99	1.09	3.45	2.25	3.18	0.15	0.78	1.25	1.56	0.88
CaO	1.04	1.08	3.36	0.51	0.63	2.40	0.10	0.06	1.23	0.40	2.06
MnO	0.02	0.04	0.02	0.27	0.01	0.06	0.01	0.02	0.01	0.01	0.28
FeO*	47.1	36.8	42.8	30.7	43.5	41.6	42.0	45.1	40.2	42.7	15.5
Na_2O	0.02	0.03	0.03	0.04	0.01	0.04	0.02	bdl	bdl	0.02	0.07
K_2O	bdl	bdl	bdl	bdl	bdl	bdl	bdl	bdl	bdl	bdl	bdl
LOI	5.07	2.76	3.83	2.67	3.86	1.91	5.8	4.83	4.66	4.15	2.32
Total	99.64	99.25	99.58	99.15	99.54	99.08	99.74	99.48	99.4	99.78	100.9

bdl below detection limit

Table 4 Mean magnetite EMP analyses (wt%)

Sample Name	Pts	SiO$_2$	TiO$_2$	Al$_2$O$_3$	Cr$_2$O$_3$	V$_2$O$_3$	Fe$_2$O$_3$	FeO	MgO	MnO	Total
BIF-1	41	0.01	0.01	0.01	0.01	0.03	68.14	30.66	0.02	0.02	98.92
		0.01	*0.02*	*0.02*	*0.01*	*0.04*	*1.30*	*0.58*	*0.03*	*0.02*	
BIF-2	23	0.06	0.07	0.69	0.01		67.55	30.39	0.01	0.01	98.78
		0.02	*0.02*	*0.17*	*0.01*		*0.18*	*0.08*	*0.02*	*0.01*	
BIF-3	43	0.07	0.01	0.07	0.01	0.02	69.18	31.12	0.02	0.01	100.51
		0.03	*0.02*	*0.02*	*0.01*	*0.03*	*0.50*	*0.22*	*0.02*	*0.02*	
BIF-4	17	0.03	0.01	0.27	0.01	0.01	69.49	31.26	0.14	0.11	101.34
		0.02	*0.02*	*0.10*	*0.02*	*0.02*	*0.60*	*0.27*	*0.04*	*0.03*	
BIF-5	48	0.08	0.01	0.01	0.01	0.00	69.89	31.45	0.02	0.01	101.49
		0.03	*0.02*	*0.02*	*0.01*	*0.00*	*0.53*	*0.24*	*0.02*	*0.02*	
BIF-6	24	0.13	1.26	0.63	0.02	0.00	68.49	30.82	0.03	0.01	101.38
		0.06	*0.66*	*0.11*	*0.01*	*0.00*	*0.82*	*0.37*	*0.02*	*0.01*	
BIF-7	16	0.19	0.01	0.16	0.01	0.01	68.72	30.92	0.02	0.02	100.05
		0.07	*0.02*	*0.03*	*0.01*	*0.02*	*0.40*	*0.18*	*0.02*	*0.02*	
BIF-8	45	0.09	0.01	0.06	0.01	0.01	69.34	31.20	0.02	0.01	100.74
		0.18	*0.02*	*0.02*	*0.01*	*0.01*	*1.25*	*0.56*	*0.02*	*0.01*	
BIF-9	44	0.07	0.01	0.03	0.01	0.03	69.46	31.25	0.03	0.01	100.89
		0.08	*0.02*	*0.02*	*0.01*	*0.04*	*0.63*	*0.29*	*0.02*	*0.01*	
BIF-10	51	0.05	0.01	0.01	0.01	0.02	69.58	31.31	0.02	0.01	101.02
		0.03	*0.02*	*0.02*	*0.01*	*0.03*	*0.54*	*0.24*	*0.02*	*0.01*	
BIF-11	38	0.18	0.26	0.58	0.02		68.64	30.88	0.07	0.03	100.67
		0.45	*0.13*	*0.26*	*0.03*		*1.37*	*0.62*	*0.04*	*0.06*	

1 σ standard deviation in italics, *blank* not measured

activity (Frost and Frost 2008). A few small seeds of Fe-rich orthopyroxene, plus Fe-rich garnet in one case, were added to a subset of the experiments in an attempt to enhance orthopyroxene growth and garnet growth in the experiment.

Each experiment was prepared by loading 1 mg of doubly distilled pure water or 1 M MgCl$_2$, 25 mg of a mineral mix, consisting of 1 part by mass coarse-grained natural magnetite from an anorthosite massif in Quebec, Canada thoroughly mixed with 2 parts by mass very fine-grained synthetic quartz into a 3 mm diameter, 1 cm long Pt capsule. To this magnetite-quartz mix was added very small amounts of MgCl$_2$, MgO, anorthite glass, and/or Al$_2$O$_3$ +/- Fe-rich orthopyroxene or garnet seeds (Table 7). The Pt capsules were pinched and arc-welded shut using an argon plasma torch. The Pt capsule seals were checked for leaks by first weighing, then placed in a 105 °C oven for 4 to 12 h, and weighed again. Only those capsules that showed no loss in weight, were used in the experiments.

Experiments were performed using a Johannes design piston-cylinder apparatus (Johannes et al. 1971; Johannes 1973) and a CaF$_2$ assembly (pressure medium) with a cylindrical graphite oven at 800 and 900 °C and 1000 MPa. Four gently flattened Pt capsules, separated by biotite sheets, were positioned vertically with the Ni-Cr thermocouple tip placed approximately halfway up alongside one of the Pt capsules in order to prevent them from welding together during the course of the experiment (cf. Angiboust and Harlov 2017). A thermal gradient exists along the length of the Pt capsules such that temperatures are 20 to 30 °C lower at the capsule tip compared to the capsule centre, which is where the temperature is actually measured. At the start of a run, the pressure was taken up to approximately 10 to 15% below the run conditions, and then the temperature was brought up to the desired value. Thermal expansion caused the pressure to increase to the approximate target value. The pressure was then adjusted to the desired value, and automatically maintained within a pre-set range (+/- 50 MPa) during the course of the entire experiment. The experiments were internally buffered to ferrosilite-magnetite-quartz, whereas the external buffer was graphite-CO$_2$ due to the graphite oven. Experiments were run for 7 to 8 days (Table 7). Quench was achieved by turning off the current, such that H$_2$O-cooling jacket cooled down the CaF$_2$ assembly to below 50 °C within about 15 to 30 s.

After quench, the capsules were cleaned, weighed, punctured, and dried in open air in a 100 °C oven for 3 to 4 h. They were weighed again in order to determine the exact fluid content. The dried, now consolidated, mineral mix was then extracted in pieces from the Pt capsule, mounted in epoxy grain mounts, and finely polished.

Point analyses of individual orthopyroxene grains (Table 8; Supplementary Appendix 2) were made with a

Table 5 Mean pyroxene EMP analyses (wt%)

Sample	Mineral	Pts	SiO$_2$	TiO$_2$	Al$_2$O$_3$	Cr$_2$O$_3$	FeO^T	MgO	MnO	CaO	Na$_2$O	Total	X$_{Fe}$	X$_{Mg}$	X$_{Mn}$	T (°C)[a]
BIF-2	Opx	46	49.43		0.61	0.01	36.41	11.78	0.09	0.72	0.01	99.05	0.633	0.365	0.002	860
			0.27		*0.12*	*0.01*	*0.56*	*0.39*	*0.03*	*0.15*	*0.01*					
	Opx exsol in Cpx	26	48.80		0.52	0.01	38.72	10.06	0.09	0.57	0.01	98.77	0.682	0.316	0.002	830
			0.30		*0.14*	*0.01*	*0.54*	*0.55*	*0.02*	*0.10*	*0.01*					
	Cpx	89	51.11	0.01	0.99	0.01	17.41	8.66	0.04	21.41	0.14	99.77	0.530	0.469	0.001	
			0.33	*0.01*	*0.07*	*0.02*	*1.19*	*0.29*	*0.02*	*1.02*	*0.02*					
BIF-3	Opx	13	51.14	0.01	0.04		35.74	12.78	0.11	0.66	0.01	100.50	0.610	0.388	0.002	885
			1.26	*0.01*	*0.03*		*2.70*	*0.65*	*0.07*	*0.16*	*0.01*					
	Cpx	35	50.68	0.01	0.02	0.01	21.64	6.74	0.07	20.53	0.25	99.95	0.642	0.356	0.002	
			0.26	*0.02*	*0.02*	*0.01*	*1.91*	*0.27*	*0.03*	*1.52*	*0.03*					
BIF-4	Opx	17	52.29	0.01	0.08	0.01	25.34	19.75	1.34	0.47	0.01	99.30	0.409	0.569	0.022	
			0.30	*0.01*	*0.04*	*0.01*	*0.31*	*0.15*	*0.06*	*0.18*	*0.01*					
BIF-5	Opx	30	52.09	0.01	0.01	0.01	37.09	10.20	0.07	0.88	0.01	100.37	0.670	0.328	0.001	
			0.41	*0.01*	*0.01*	*0.02*	*0.91*	*0.14*	*0.03*	*0.21*	*0.01*					
	Augite	5	54.14		0.02	0.01	22.89	11.48	0.03	11.42	0.07	100.06	0.528	0.472	0.001	
			0.30		*0.02*	*0.02*	*0.24*	*0.11*	*0.02*	*0.06*	*0.03*					
BIF-6	Opx	38	47.42	0.01	0.24	0.01	44.81	6.45	0.08	0.52	0.01	99.56	0.795	0.204	0.001	775
			0.33	*0.02*	*0.04*	*0.01*	*0.66*	*0.11*	*0.03*	*0.05*	*0.02*					
	Cpx	18	50.22	0.01	0.63	0.01	22.31	5.65	0.03	20.21	0.63	99.69	0.688	0.311	0.001	
			0.43	*0.01*	*0.07*	*0.01*	*0.51*	*0.10*	*0.02*	*0.37*	*0.05*					
BIF-8	Opx	23	54.55	0.02	0.01	0.01	28.52	16.41	0.26	0.24	0.02	100.04	0.491	0.504	0.005	
			0.22	*0.02*	*0.01*	*0.02*	*0.44*	*0.24*	*0.04*	*0.08*	*0.02*					
BIF-9	Opx	19	53.84	0.01	0.02	0.01	31.50	14.29	0.11	0.64	0.01	100.42	0.552	0.446	0.002	
			0.65	*0.01*	*0.02*	*0.02*	*0.51*	*0.35*	*0.02*	*0.05*	*0.01*					
BIF-10	Opx	36	52.93	0.01	0.01	0.01	33.44	12.87	0.08	0.59	0.01	99.94	0.592	0.406	0.001	
			0.38	*0.01*	*0.01*	*0.01*	*1.10*	*0.61*	*0.03*	*0.07*	*0.01*					
BIF-11	Opx	2	49.27		0.52		34.78	12.53	2.27	0.44		99.81	0.585	0.376	0.039	880
			0.15		*0.27*		*0.40*	*0.14*	*0.01*	*0.04*						
	Opx exsol in Cpx	21	47.62	0.01	0.95		38.52	8.33	3.16	0.97	0.01	99.56	0.681	0.263	0.057	815
			0.34	*0.01*	*0.10*		*0.69*	*0.30*	*0.12*	*0.61*	*0.01*					
	Cpx	23	50.85	0.01	1.57	0.01	18.57	7.72	1.01	20.86	0.49	101.09	0.557	0.413	0.031	
			0.57	*0.01*	*0.22*	*0.02*	*1.21*	*0.59*	*0.34*	*0.96*	*0.05*					

1 σ standard deviation in italics, *blank* measured but not detected

[a]Opx-Cpx thermometer, Brey and Köhler (1990)

JEOL JXA-8230 EMP with four wavelength-dispersive spectrometers (WDS) at the Centre for Global Tectonics, School of Earth Sciences, China University of Geosciences, Wuhan, China. The operating conditions included a 15 kV accelerating voltage, a 20 nA probe current, and a 1 to 3 µm beam diameter. Measuring times were 10 s on element peaks

Table 6 Mean garnet EMP analyses (wt%)

Sample	Pts	SiO$_2$	TiO$_2$	Al$_2$O$_3$	FeO^T	MgO	MnO	CaO	Total	X$_{Fe}$	X$_{Mg}$	X$_{Mn}$	X$_{Ca}$	T (°C)[a]	T (°C)[b]
BIF-6	17	36.50	0.01	19.93	34.72	0.96	0.26	7.20	99.59	0.756	0.037	0.006	0.201	760	840
		0.14	*0.02*	*0.20*	*0.61*	*0.05*	*0.03*	*0.13*							
BIF-11	26	37.28	0.01	20.15	28.46	1.80	5.67	7.35	100.7	0.608	0.068	0.123	0.201	945	1055
		0.15	*0.01*	*0.17*	*0.26*	*0.20*	*0.34*	*0.35*							

1 σ standard deviation in italics

[a]Gt-Opx thermometer, Lee and Ganguly (1988)

[b]Gt-Cpx thermometer, Berman et al. (1995)

Table 7 Summary of BIF metasomatism experiments

Experiment	T(°C)	P(MPa)	Time (days)	H_2O	1 M $MgCl_2$	$MgCl_2$	MgO	An glass	Al_2O_3	Grt seeds	Opx seeds
Exp BIF-14	800	800	7		1.1	0.78					
Exp BIF-15	800	800	7		1.17	1.2		added		added	added
Exp BIF-18	900	1000	8	1.13		2		added			added
Exp BIF-20	900	1000	8	1.13			2	added			added
Exp BIF-21	900	1000	8	1.03			2		added		added

All amounts in mg except for the MgO, An glass, Al_2O_3, Fe-rich Grt seeds, and Fe-rich Opx seeds, which were added in trace amounts

and half that on background locations adjacent to peaks. For both sets of EMP analyses, raw X-ray intensities were corrected using a ZAF (atomic number, absorption, fluorescence) correction procedure. Natural and synthetic silicates, oxides, and phosphate standards were used for calibration. Matrix corrections were performed using software supplied by JEOL. In order to ensure that the relative differences observed were correct to within the EMP error, all analyses per sample were obtained during one single measuring session including multiple checks of the calibration.

Results

Whole rock chemistry

The whole-rock chemistry of the BIF (Table 3; Fig. 4) demonstrates that FeO varies from 15.51 to 47.05 wt.% and SiO_2 from 44.50 to 78.20 wt.%; these values are comparable to those of Archean BIFs worldwide (Alexander et al. 2008). The MgO content is lower and varies from 0.15 to 3.45 wt.% (Fig. 4b) with **BIF-4** having the highest value. The Al_2O_3 content in all samples is low, ranging up to a maximum of 1.73 wt.% (in garnet-bearing **BIF-6**) (Fig. 4a). The CaO content in the clinopyroxene- (**BIF-2**, **BIF-3**) and

garnet-bearing (**BIF-6**, **BIF-11**) samples ranges from 1.08 to 3.36 wt.% (Fig. 4d).

Mineral textures and chemistry

Several polished thin sections each of BIF samples 1 through 11 (Figs. 2 and 5) were prepared and examined under the petrographic microscope in order to document the mineral assemblages and associated textures (Table 2). Principal minerals include fine- to coarse-grained (0.1–1 mm), subhedral to anhedral magnetite and quartz along with lesser amounts of subhedral to anhedral orthopyroxene, +/- clinopyroxene, +/- amphibole, +/- garnet, and +/- plagioclase along magnetite-quartz grain boundaries.

BIF-1 (Fig. 5a) has a plumose structure that formed during mylonitization. Both magnetite (Table 4) and quartz are fine-grained, though the magnetite grains are coarser than the quartz. There is a weak alternate banding between the magnetite and quartz. Actinolite-tremolite (Table 2) occurs along magnetite-quartz grain boundaries (Fig. 5a); no pyroxenes were found.

Although **BIF-2** and **BIF-11** come from the same locality (Fig. 2), the samples differ in their mineralogy. **BIF-2** consists of magnetite-quartz-orthopyroxene-clinopyroxene (Fig. 5b; Tables 2 and 4). The orthopyroxene ($X_{Fe} = 0.633$) and clinopyroxene ($X_{Fe} = 0.530$; Table 5) are coarse grained.

Table 8 Orthopyroxene EMP analyses from the metasomatic experiments

Experiment	#pts	SiO_2	TiO_2	Al_2O_3	Cr_2O_3	FeO^T	MgO	MnO	CaO	Total	X_{Fe}	X_{Mg}	X_{Mn}	X_{Al}
Exp BIF-14	20	54.11	0.07	1.07	0.02	19.54	24.91	0.24	0.45	100.42	0.304	0.692	0.004	0.012
		0.89	*0.04*	*0.45*	*0.02*	*2.19*	*2.08*	*0.15*	*0.51*					
Exp BIF-15	16	52.89	0.04	3.67	0.02	18.02	25.96	0.09	0.11	100.81	0.280	0.719	0.001	0.039
		1.48	*0.05*	*2.00*	*0.03*	*1.37*	*1.18*	*0.11*	*0.15*					
Exp BIF-18	25	49.28	0.02	10.71	0.02	16.05	25.43	0.01	0.05	101.57	0.261	0.738	0.000	0.109
		0.75	*0.02*	*0.67*	*0.02*	*0.71*	*0.67*	*0.01*	*0.02*					
Exp BIF-20	18	55.58	0.02	1.39	0.01	16.24	27.20	0.05	1.21	101.71	0.251	0.749	0.001	0.015
		0.68	*0.02*	*0.56*	*0.02*	*2.83*	*2.25*	*0.05*	*1.43*					
Exp BIF-21	14	50.11	0.03	9.95	0.02	16.54	24.47	0.02	0.03	101.18	0.275	0.725	0.000	0.104
		1.86	*0.03*	*1.28*	*0.02*	*1.11*	*1.06*	*0.02*	*0.06*					

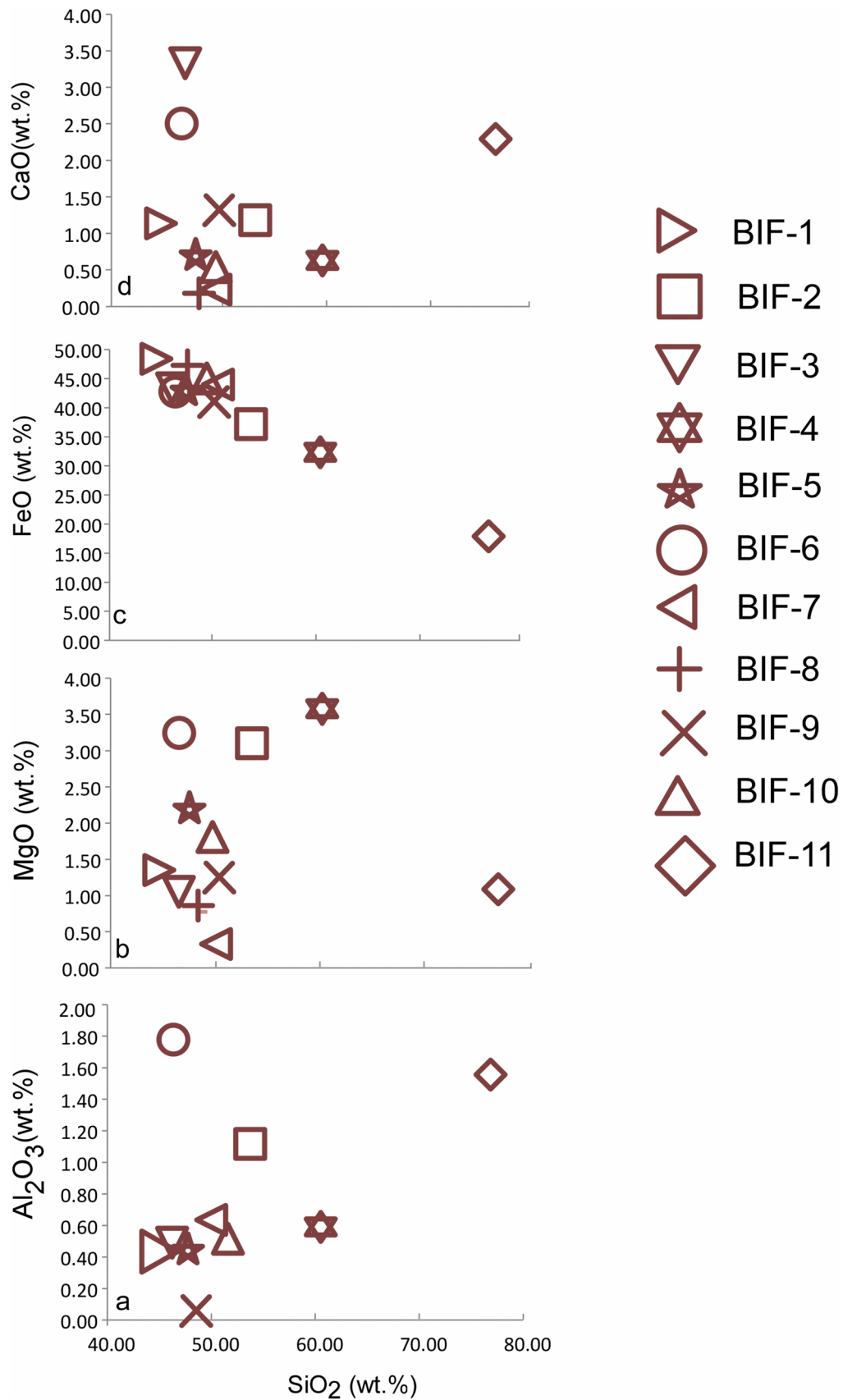*1 σ* standard deviation in italics

Fig. 4 Harker plots showing whole-rock composition of each of the BIF samples in wt.%. **a** SiO$_2$ vs. Al$_2$O$_3$. **b** SiO$_2$ vs. MgO. **c** SiO$_2$ vs. FeO. **d** SiO$_2$ vs. CaO

Fig. 5 High-contrast BSE images showing varied textures and mineral assemblages of granulite-grade metamorphosed BIFs in the Kolli Massif. **a** Effect of shearing on magnetite and quartz with a total absence of orthopyroxene and clinopyroxene in sample **BIF-1**. **b** Co-existing orthopyroxene-clinopyroxene with magnetite and quartz in sample **BIF-2**. **c–e** Co-existing orthopyroxene-magnetite-quartz assemblages in samples **BIF-3**, **BIF-4**, and **BIF-5**. **f** Co-existing garnet-clinopyroxene with magnetite and quartz in sample **BIF-6**. **g** Magnetite-quartz texture showing a total absence of orthopyroxene and clinopyroxene reaction textures in sample **BIF-7**. **h–j** Co-existing orthopyroxene-magnetite-quartz assemblages in samples **BIF-8**, **BIF-9**, and **BIF-10**. **k**, **l** co-existing garnet-clinopyroxene with magnetite and quartz in sample **BIF-11**. Mag - magnetite, Opx - orthopyroxene, Cpx - clinopyroxene, Qz - quartz, Grt - garnet, Ap - apatite, Amp - amphibole, Pl - plagioclase, Kfs - K-feldspar
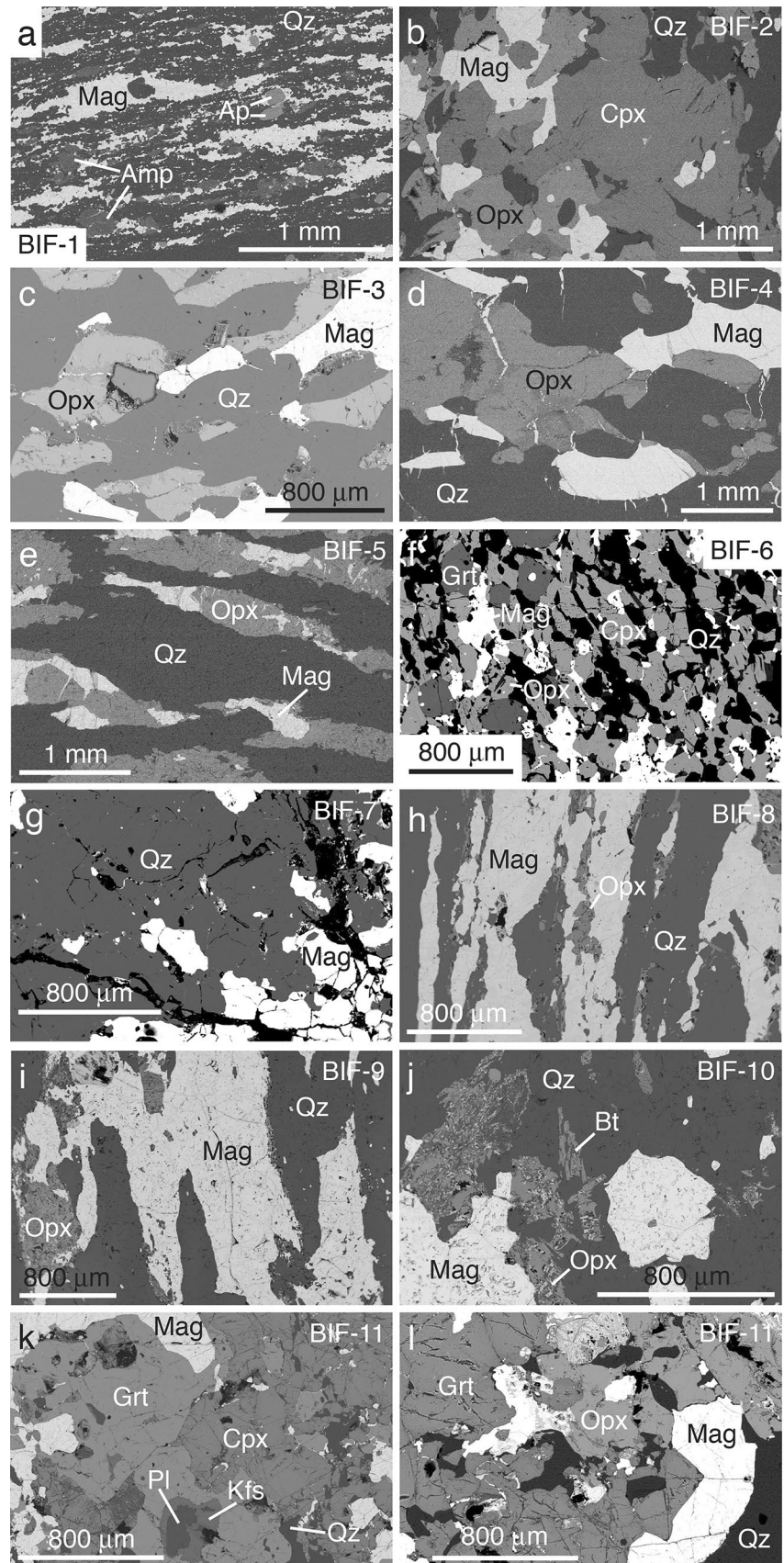
The clinopyroxenes have thin exsolution lamellae of orthopyroxene ($X_{Fe} = 0.682$; Table 5), which are parallel to the [100] lattice plane (Fig. 6). **BIF-11** has the assemblage magnetite-quartz-orthopyroxene-clinopyroxene-garnet-plagioclase. The mineral grains are small and appear to be recrystallized (Fig. 5k, l). In **BIF-11** the garnet ($X_{Fe} = 0.608$; Table 6) and clinopyroxene ($X_{Fe} = 0.557$; Table 5) occur along magnetite-quartz grain boundaries (Fig. 5k). Clinopyroxenes are weakly overprinted by retrograde amphibole. This sample also contains minor orthopyroxene ($X_{Fe} = 0.585$; Table 5). The pyroxenes have no resorbed boundaries or reaction rims. The garnet contains inclusions of K-feldspar, which in turn hosts albite inclusions (Fig. 5k). The clinopyroxene grains have thin exsolution lamellae of

Fig. 6 BSE image of orthopyroxene lamellae along the [100] lattice plane in clinopyroxene from sample **BIF-2**. Mineral abbreviations the same as for Fig. 5
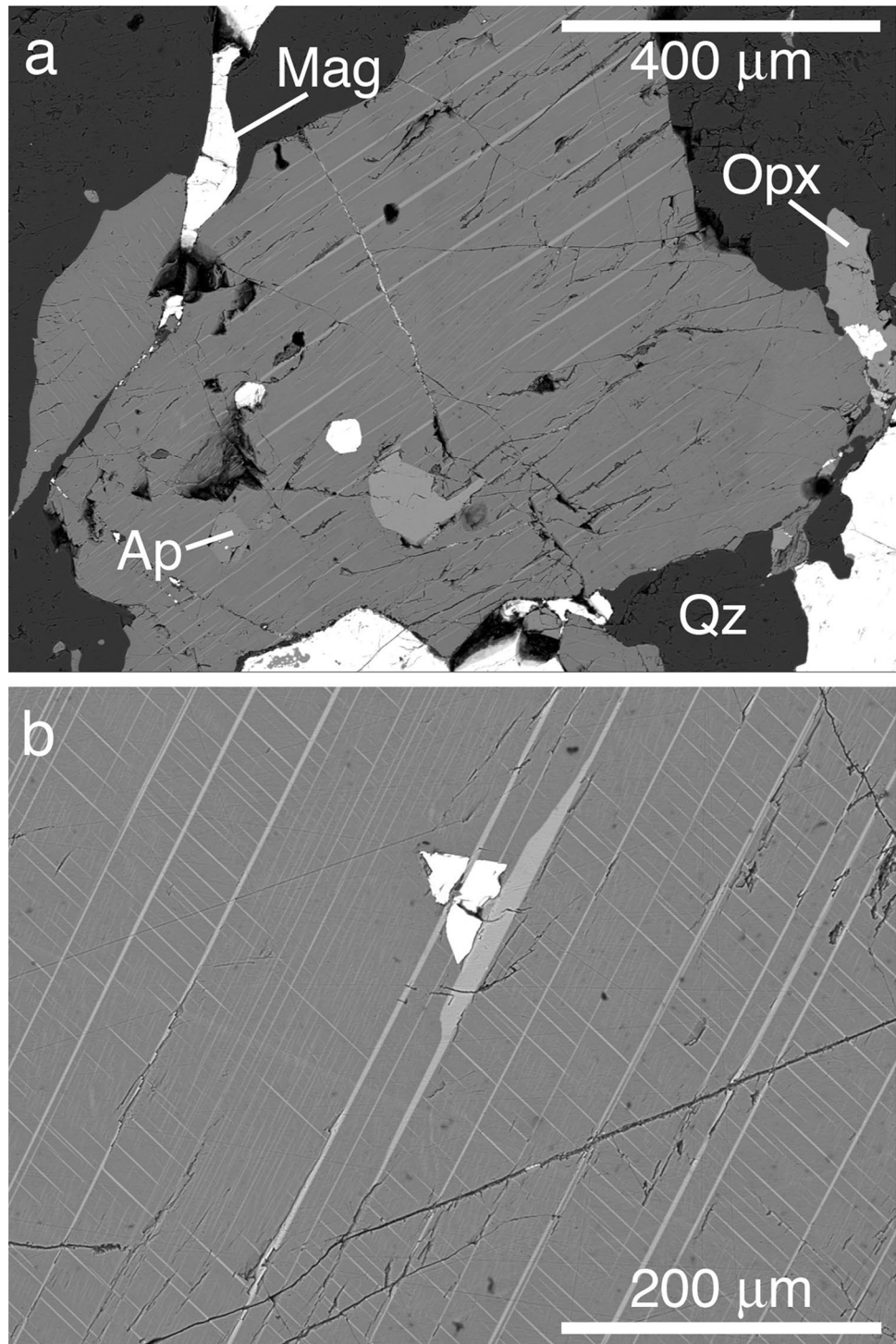
orthopyroxene ($X_{Fe} = 0.681$, Table 5) that are parallel to the [100] lattice plane similar to that seen for **BIF-2** (Fig. 6).

BIF-3 contains magnetite-quartz-clinopyroxene-orthopyroxene with no obvious textural orientation (Table 2 and 4). The orthopyroxene ($X_{Fe} = 0.610$; Table 5) occurs along quartz-magnetite grain boundaries, has no resorbed boundaries or reaction rims, and is coarse-grained (Fig. 5c). Clinopyroxene occurs locally ($X_{Fe} = 0.642$; Table 5), but is not associated with the orthopyroxene. It contains no clinopyroxene exsolution lamellae.

BIF-4 contains coarse-grained magnetite-quartz-orthopyroxene (Tables 2 and 4). The orthopyroxenes ($X_{Fe} = 0.409$; Table 5) occur along magnetite-quartz grain boundaries (Fig. 5d).

BIF-5 consists of magnetite-quartz-orthopyroxene-augite with weak alternating bands of quartz and magnetite (Fig. 5e; Tables 2 and 4). The coarse-grained orthopyroxene ($X_{Fe} = 0.670$; Table 5) forms along magnetite-quartz grain boundaries along with rare augite ($X_{Fe} = 0.528$; Table 5).

BIF-6 has a granular garnet-clinopyroxene-orthopyroxene reaction texture along magnetite-quartz grain boundaries (Fig. 5f; Tables 2 and 4). The clinopyroxene ($X_{Fe} = 0.688$; Table 5), orthopyroxene ($X_{Fe} = 0.795$; Table 5), and garnet ($X_{Fe} = 0.756$; Table 6) is enriched in Fe. The clinopyroxene contains no orthopyroxene exsolution lamellae.

BIF-7 is slightly altered and contains no Fe-Mg silicate minerals (Tables 2 and 4). Both the magnetite and quartz are coarse grained and show no indications of alternate banding (Fig. 5g).

BIF-8 (Fig. 5h) and **BIF-9** (Fig. 5i) are characterized by coarse-grained magnetite-quartz-orthopyroxene-amphibole (Tables 2 and 4). Orthopyroxene in **BIF-9** is slightly more Mg-rich ($X_{Fe} = 0.552$; Table 5) than in **BIF-8** ($X_{Fe} = 0.491$; Table 5). The orthopyroxene forms reaction textures along magnetite and quartz grain boundaries (Fig. 5h, i). In both samples, the orthopyroxene is locally partially replaced by late-stage amphibole.

Texturally **BIF-10** consists of coarse-grained magnetite and quartz (Fig. 5j). Orthopyroxene ($X_{Fe} = 0.592$; Table 5) occurs along magnetite-quartz grain boundaries and as sporadic elongate grains in the quartz matrix.

P-T calculations

Considering the presence of co-existing orthopyroxene-clinopyroxene-garnet, there are a number of possible Fe-Mg exchange geothermometers that can be applied. These include orthopyroxene-clinopyroxene (Brey and Köhler 1990), garnet-orthopyroxene (Lee and Ganguly 1988), and garnet-clinopyroxene (Berman et al. 1995). Assuming an approximate regional pressure of around 1000 MPa (Chowdhury and Chakraborty 2019; Dutta et al. 2022), the orthopyroxene-clinopyroxene geothermometer indicates a temperature range of around 800 to 850 °C for BIF samples

containing orthopyroxene and clinopyroxene (cf. Table 5). For the two garnet-bearing samples, temperatures of 760 and 945 °C (garnet-orthopyroxene thermometer) and 840 and 1055 °C (garnet-clinopyroxene thermometer) were obtained for BIF-2 and BIF-11, respectively (Table 6). The low Al contents in orthopyroxene did not allow for the Al-in-orthopyroxene barometer of Brey and Köhler (1990) to be applied. This would appear to be due to the low Al content in the whole rock chemistry of these BIFs (Table 2). These temperatures are in broad agreement with the estimated regional temperatures estimated (see above) and with temperatures in the phase equilibria modelling (Fig. 7).

Phase-equilibria modelling

A *P-T* pseudo-section for the system SiO_2-Al_2O_3-FeO-MgO-CaO-O_2 was calculated from the bulk composition of **BIF-2** using *Perple-X* 6.8.4 (Table 3; Supplementary Appendix 3.1; Fig. 7) as a function of pressure and temperature using the Gibbs free energy minimization technique (Connolly 2005) and the thermodynamic data set and mineral solution models contained in Holland and Powell (1998) (Supplementary Appendix 3.2). The input DAT file can be found in Supplementary Appendix 3.3. No melt phase occurs over the *P-T* range considered. The computed pseudo section in Fig. 7 agrees with the high *P-T* mineral assemblage found in the sample and shows that the magnetite-quartz-orthopyroxene-clinopyroxene assemblage has a wide *P-T* stability field ranging from over ~400 MPa and ~600 °C (more details about the pseudo-section are included in the figure caption).

Experimental replication of reaction textures

Orthopyroxene reaction textures along magnetite-quartz grain boundaries were obtained in a series of the BIF experiments run at 800 °C and 800 MPa and at 900 °C and 1000 MPa (Tables 7 and 8; Supplementary Appendix 2; Fig. 8). No garnet, clinopyroxene, or amphibole formed in any of these experiments. Voids seen between minerals and along mineral grain boundaries in Fig. 8 were once filled with Mg- and Al-bearing saline to hypersaline fluids.

The orthopyroxene that formed tends to be relatively rich in Mg compared to Fe with somewhat variable amounts of Al from experiment to experiment (Table 8). The EMP analytical results reported in Table 8 are mean values taken from a series of individual single grain point analyses, i.e. one analysis per grain (Fig. 8). The high standard deviations seen for these mean values indicate that there is a relatively high variability in the Fe, Mg, and Al contents between the orthopyroxene grains in each of the experiments (Supplementary Appendix 2). Compared to the composition of orthopyroxene grains from the natural samples (Table 5), the Mg contents are considerably higher

Fig. 7 *P-T* pseudo-section in the system SiO$_2$–Al$_2$O$_3$–FeO–MgO–CaO–O$_2$ (55.32–1.09–37.43–3.03–1.09–2 wt.%) calculated from the bulk composition of **BIF-2** (see Table 2). The magnetite-quartz-orthopyroxene-clinopyroxene assemblage of this sample is stable above 400 MPa and 600 ℃. The isopleths generated from the respective orthopyroxene and clinopyroxene solution models are very closely spaced and are not included in the diagram. The arrow marked shows the *P-T* path of the exhumation of the BIFs that led to the formation plagioclase during decompression

$$SiO_2:55.32, Al_2O_3:1.09, FeO:37.43, MgO:3.03, CaO:1.09, O_2:2$$
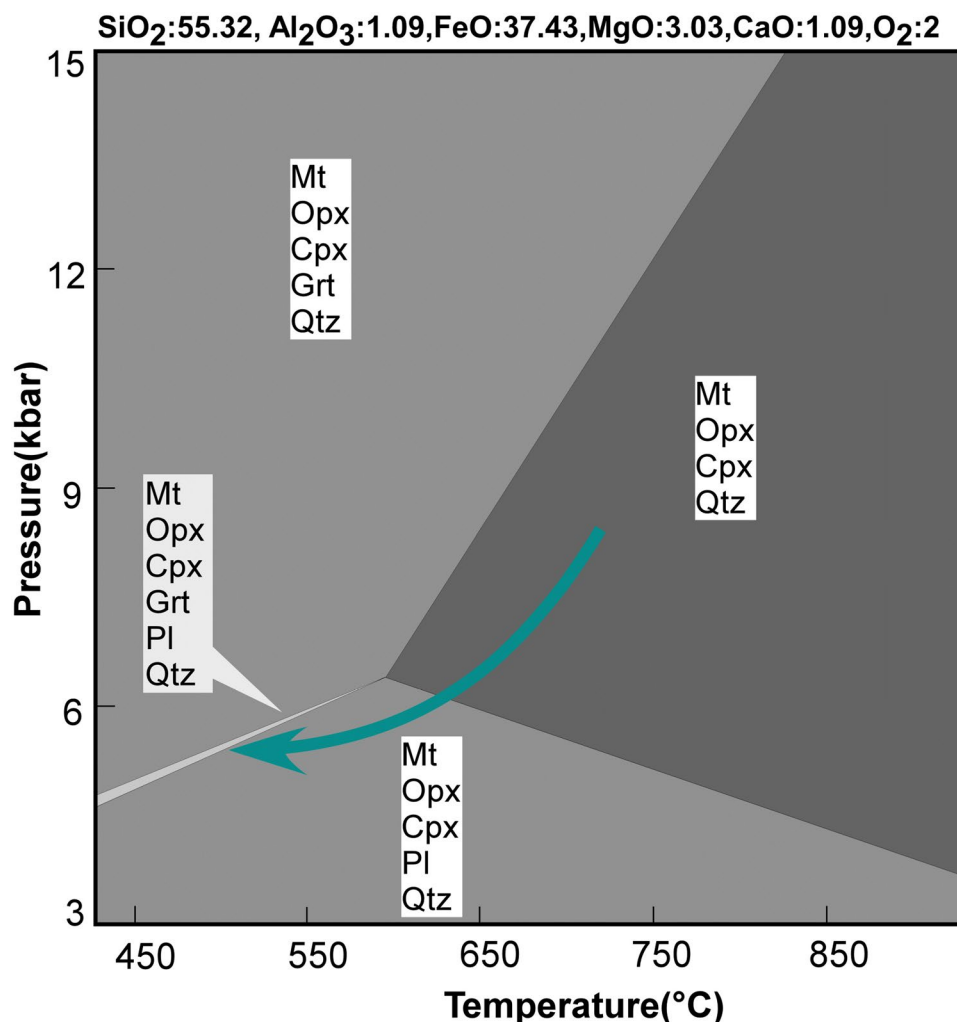
in the experimentally grown orthopyroxenes for all of the experiments, whereas the Al contents in the orthopyroxene are higher for two of the experiments at 900 °C and 1000 MPa at around 10 wt% Al$_2$O$_3$ (Table 8; Supplementary Appendix 2). The high Al$_2$O$_3$ values in these orthopyroxene grains are probably due to the high *P-T* of the experiments and to the fact that the amount of Al added was apparently much higher than in the other three experiments conducted under the same *P-T* conditions. Such high Al-orthopyroxenes with similar Al$_2$O$_3$ values are commonly found in Al-rich rocks, which have experienced a pressure-temperature regime similar to those seen in the experiments, i.e. 900 °C and 1000 MPa (cf. Kienast and Ouzegane 1987; Harley and Motoyoshi 2000; Kelly and Harley 2004; Sajeev and Osanai 2004; Belyanin et al. 2012; Scribano and Carbone 2020).

A series of initial experiments at 700, 800, and 900 °C and 1000 to 1400 MPa, which involved similar proportions of magnetite and quartz, were done for time periods ranging from 11 to 28 days. These experiments were either fluid-free, i.e. charge dried at 600 °C or dry at 25 °C with residual

atmospheric moisture, or with small amounts (1–2 mg) H$_2$O or 1 M HCl added. In the case of the 1 M HCl experiments, +/- 0.1–0.5 mg amounts of anorthite glass, +/- Fe-rich orthopyroxene seed crystals, +/- Fe-rich clinopyroxene seed crystals, and/or +/- Fe-rich garnet seed crystals were added. None of these experiments resulted in Fe-Mg silicate minerals forming either independently or as reaction textures along the magnetite-quartz grain boundaries. Rather the magnetite-quartz grain boundary interface was very clean with no evidence of any kind of reaction or alteration.

Discussion

Origin and evolution of oxide-silicate mineral textures in the BIFs

The high-grade BIFs of the Kolli Massif are characterized by the presence of several, various reaction textures. Each individual BIF enclave, lens, or layers may be considered

to be an open chemical system in which mass transfer of elements between the BIF and the surrounding rocks took place during metamorphism, most likely enhanced by fluid-aided transport.

In **BIF-1**, the actinolite-tremolite ($Ca_2(Mg,Fe^{2+})_5Si_8O_{22}(OH)_2$–$Ca_2Mg_5Si_8O_{22}(OH)_2$) (Table 2; Fig. 5a) possibly developed through the metasomatic alteration of previously formed clinopyroxene (see below). However, the lack of any relict clinopyroxene in the sample, specifically associated with the amphibole, suggests that these amphiboles were a direct reaction product of the original magnetite and quartz coupled with the fluid-aided infiltration of Ca and Mg via the following generalized reaction:

$$Fe_3O_4 + SiO_2 + MgO \ (in \ fluid)$$
$$+ \ CaO \ (in \ fluid) + H_2O = (Ca_2(Mg, Fe^{2+})_5Si_8O_{22}(OH)_2 \quad (1)$$
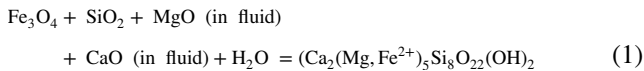
This reaction was most likely generated during greenschist facies metamorphism due to fluid interaction between the magnetite-quartz layers and surrounding country rock, which would have taken place during post-peak *P-T* exhumation and cooling under a relatively high H_2O activity.

In the case of the orthopyroxene-bearing BIF samples (**BIF-8**, **BIF-9**, and **BIF-10**) (Table 2; Fig. 5h–j) the orthopyroxene predictably formed as a reaction product between magnetite and quartz via the generalized reaction:

$$Fe_3O_4 + SiO_2 + MgO \ (in \ fluid)$$
$$+ \ Al_2O_3 \ (in \ fluid) = (Fe, Mg)_2(Si, Al)_2O_6 + O_2. \quad (2)$$
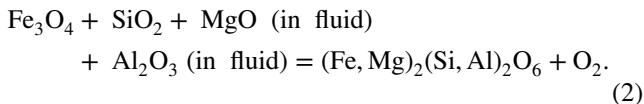
under a low H_2O activity, and presumably low K_2O and TiO_2 activity, as evidenced by the lack of high-grade (high Ti) biotite either prograde or retrograde. In these samples, the relatively low Al content in the orthopyroxenes ($< 1\%$ Al_2O_3 wt%) (Table 5) seems reflective of the low Al content in the BIF overall, (i.e. low Al_2O_3 activity), and not due to formation at low temperatures (see discussion in Harlov et al. (2006)).
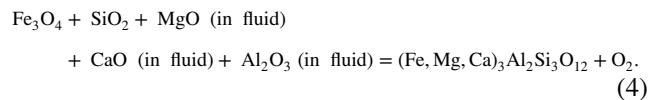
Co-existing clinopyroxene-orthopyroxene textures in **BIF-2**, **BIF-3**, **BIF-4**, **BIF-5**, **BIF-6**, and **BIF-11** (Table 2; Figs. 5b–e) indicate coeval formation from the original magnetite and quartz assisted by the infiltration of the same elements for orthopyroxene, but with the addition of sufficient amounts of CaO, via the generalized reaction:

$$Fe_3O_4 + SiO_2 + MgO \ (in \ fluid)$$
$$+ \ CaO \ (in \ fluid) + Al_2O_3 \ (in \ fluid) = Fe_2Si_2O_6 + Ca(Fe, Mg)(Si, Al)_2O_6 + O_2. \quad (3)$$
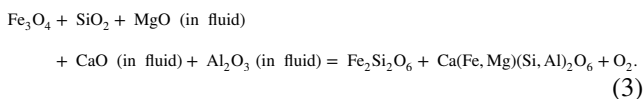
The presence of orthopyroxene exsolution lamellae within the clinopyroxene parallel to the [100] lattice plane in **BIF-2** (Fig. 6) indicates a solid-state, sub-solidus exsolution of orthopyroxene during slow cooling of the clinopyroxene. Orthopyroxene, both as lamellae and as blebs within clinopyroxene, is a characteristic of clinopyroxenes from a

high *P-T* BIF (Harley 1987). Clinopyroxene forms a solid solution with minor amounts of orthopyroxene at 1000 to 1100 MPa and $\geq$ 900 °C (Fonarev et al. 2006). The orthopyroxene lamellae would have exsolved at temperatures below 800 °C, which is consistent with the thermodynamic modelling (Fig. 7). The lack of biotite formation in these orthopyroxene-clinopyroxene-bearing BIFs again would appear to be a combination of both a low H_2O activity, coupled with a low activities K_2O, Al_2O_3, and low TiO_2 activity in these BIFs (Table 3) during both their prograde and retrograde tectonic history.

Whole-rock data for the garnet-orthopyroxene-clinopyroxene-bearing samples (**BIF-6, BIF-11**) indicate they are relatively rich in Ca and Al (CaO = 2.06–2.40 wt%; $Al_2O_3 = 1.44$–1.73 wt%; Tables 2 and 3; Figs. 4 and 5f, k, l). This is confirmed by the presence of plagioclase in **BIF-11**, which must have formed with the aid of external fluids, and allowed for the formation of Fe-rich garnet from magnetite and quartz via the following possible generalized reaction:

$$Fe_3O_4 + SiO_2 + MgO \ (in \ fluid)$$
$$+ \ CaO \ (in \ fluid) + Al_2O_3 \ (in \ fluid) = (Fe, Mg, Ca)_3Al_2Si_3O_{12} + O_2. \quad (4)$$

The clinopyroxene in **BIF-6** does not contain orthopyroxene exsolution lamellae, which suggests they formed at temperatures below 800 °C, which is in good agreement with its orthopyroxene-clinopyroxene temperature of 775 °C (Table 5). The clinopyroxene in **BIF-11** (and **BIF-2** collected a few meters away) has orthopyroxene exsolution lamellae (Fig. 6). This agrees well with their higher orthopyroxene-clinopyroxene temperatures of 860 and 880 °C, respectively (Table 5). An exception here is **BIF-3**, which has an orthopyroxene-clinopyroxene temperature of 885 °C, despite having no orthopyroxene lamellae in the clinopyroxene.

Of particular interest is **BIF-7** (Fig. 5g) in which no silicate reaction minerals formed, but which experienced the same high-grade metamorphism as the other BIF samples in this study. The most likely explanation for this lack of reaction textures would be the near-total lack of any fluids in either the BIF or the surrounding rock. This would greatly retard any element mass transfer between the BIF and the surrounding rock. This could also be coupled with the fact that, with the exception of FeO and SiO_2, all other elements existed only in trace amounts in the original chemical sediment responsible for the BIF (Table 3). Without the presence of fluids to facilitate mineral reactions, the chances of no reaction occurring between mineral phases in physical contact are quite high even under the high-grade *P-T* conditions experienced by this BIF allowing for the persistence of metastable mineral assemblages (see discussion in Harlov and Newton 1993; Harlov and Milke 2002; Harlov et al. 2008; Kihle et al. 2010).
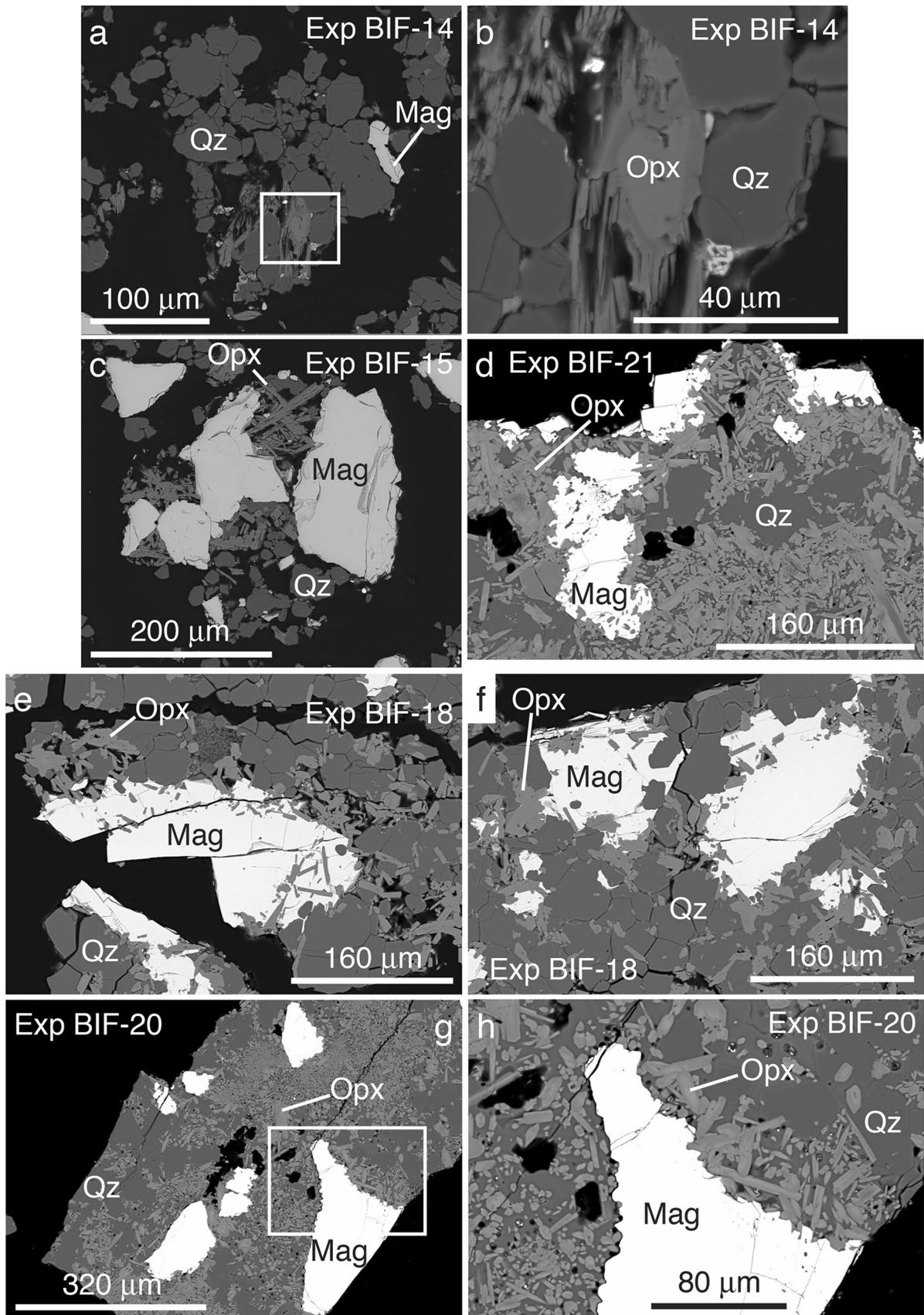
◀**Fig. 8** High-contrast BSE images from several BIF reaction experiments showing orthopyroxene reaction textures associated with magnetite. These include **a–c** BIF-14 and **BIF-15** at 800 °C and 800 MPa and **d–h** **BIF-18**, **BIF-20**, and **BIF-21** at 900 °C and 1000 MPa (Table 8). **b** is an enlargement of the outlined area in **a**. **h** is an enlargement of the outlined area in **g**. In each of these experiments, orthopyroxene grew as a reaction product from magnetite, quartz, $MgCl_2$, and Al_2O_3 via reaction (2). Mineral abbreviations the same as for Fig. 5

Comparisons between natural and experimentally-produced reaction textures

The *P-T* estimates of the various natural BIFs are reflected by the experimental *P-T* conditions (800–1000 MPa, 800–900 °C), in which the orthopyroxene reaction textures along magnetite-quartz grain boundaries were replicated (Fig. 8) similar to that seen in samples **BIF-8**, **BIF-9**, and **BIF-10** (Fig. 5h–j). In these experiments it is clear that the formation of orthopyroxene is not a simple matter of a reaction between magnetite and quartz. Rather it requires additional elements. This is because the stability field of orthopyroxene is a function of the Al and Mg content in addition to the *P-T* conditions (cf. Frost and Frost 2008). This is certainly indicated by the composition of the orthopyroxenes, which formed during the experiments (Tables 7 and 8). Earlier, fluid-absent experiments to which no external elements were added to the magnetite-quartz matrix resulted in no reaction textures forming at all at 700, 800, or 900 °C and 1000 to 1200 MPa even after 28 days. This was also the case if the fluids contained only H_2O or were HCl-solutions. The presence of a $MgCl_2$ hypersaline solution along the magnetite-quartz grain boundaries in addition to promoting the formation of orthopyroxene also guaranteed that the H_2O activity of the system was low enough such that orthopyroxene would be a stable phase under the *P-T* conditions of the experiments.

The implication from these experiments is that the BIF layers, enclaves, and lenses covered in this study, with one exception (**BIF-7**), were not closed systems, but rather were subjected to an influx of Na, Ca, K, Al, Mg, Mn, etc. during high-grade metamorphism and post-peak uplift and cooling. It is also possible that their original Fe-rich chemical sedimentary protoliths not only consisted of Fe and Si, but were also contaminated with minor amounts of Mg-, Ca-, and Al-bearing detrital/chemical sediments that were deposited along with the Fe and Si oxides/hydroxides. This would account for the formation of additional minerals as reaction textures associated with magnetite and quartz in these BIFs, such as orthopyroxene, clinopyroxene, and garnet, and the formation of plagioclase and K-feldspar independent of the magnetite and quartz (Table 2; Fig. 5k). In the experiments, orthopyroxene growth was facilitated by the presence of a saline to hypersaline $MgCl_2$ fluid along

grain boundaries along with an Al source (Tables 7 and 8; Fig. 8). Such a fluid with an $MgCl_2$ and Al component (possibly as $AlCl_3$), in tandem with other elements complexing as chlorides, could have been present during the high-grade metamorphism of these pyroxene-bearing and pyroxene-garnet-bearing BIFs. They would have originated from the surrounding rocks, all of which are both Mg- and Al-bearing. The fact that biotite did not form in any of the BIF layers, enclaves, and lenses described in this study would support the idea that these fluids had a low H_2O activity, which would be one of the characteristics of a hypersaline fluid, similar to the fluids present in the experiments, coupled with a probable low K_2O activity (with perhaps one exception - **BIF-11** (cf. Table 2)). The presence of amphibole only in **BIF-1** and its total absence in the orthopyroxene-only-bearing BIFs and the other BIFs can be treated as being due to the higher H_2O activities under probable mid-crustal, greenschist-facies conditions during uplift and cooling.

Geodynamic implications for the formation of metamorphic BIF in the Archean Kolli Massif

The relationship of the BIF layers with their surrounding rocks is not easy to determine considering the multiple deformation history of the Kolli Massif. The metamorphosed BIFs in this study are in contact with granulite-facies gneisses, meta-gabbros, pyroxenites, websterites, and rarely two-pyroxene granulites. The Kolli Massif experienced high-grade metamorphism ranging from granulite- to eclogite-facies towards the end of the Archean (Subramaniam 1956; Mukhopadhay and Bose 1994; Bhaskar Rao et al. 1996; Sajeev et al. 2009; Anderson et al. 2012; Ram-Mohan et al. 2013; Noack et al. 2013). The BIFs covered in this study occur as enclaves, lenses, and extensive layers ranging from a few meters to several kilometres in length and from cms to 200 to 300 m in width. The two major questions to address here are: 1) what processes brought these meta-sedimentary iron formations and the surrounding meta-igneous rocks together, and 2) what is the significance of these processes with respect to the time of their formation?

Field observations indicate that the BIFs commonly strike E-W and dip sub-vertically following the general regional trend. The fact that the BIFs originated as meta-sediments, and the widespread occurrence of now mostly thin, calc-silicate marbles throughout the Kolli Massif (up to 250 m wide and 32 km long at Sankagiri - Fig. 2), suggest a shallow marine environment, probably on a passive continental/arc margin (Bradley 2008; Bekker et al. 2010; Satish-Kumar et al. 2021); however, their current presence as layers in and bordering meta-igneous rocks that have HP assemblages is indicative of deep subduction (e.g. Sajeev et al. 2009; Sato et al. 2011; Noack et al. 2013; George et al. 2019).

Previous studies of the Kolli Massif suggested a history of subduction of sediments followed by arc magmatism towards the end of the Archean (Rajesh 2012; Ram-Mohan et al. 2013; George et al. 2019). However, the details of how this subduction occurred and the geometry involved are still hotly debated (Noack et al. 2013; Sengupta et al. 2015; Chowdhury and Chakraborty 2019; Santosh 2020; Dutta et al. 2022), and are beyond the scope of this study.

The predominant rocks in contact with the BIFs are orthogneisses (as shown in Fig. 2) with a TTG composition (Rajesh 2012; Tomson et al. 2013; Glorie et al. 2014). The BIF lenses, enclaves, and layers are relicts within them. We consider that the protoliths of the Kolli Massif orthogneisses were most likely intruded in batholithic proportions into the BIF-bearing sedimentary package in an active continental margin setting, as also reported by Yellappa et al. (2016). An active plate margin would imply subduction of an oceanic plate with shallow marine sediments, and an island arc, which were taken down to granulite- to eclogite-facies depths (≥ 800 °C; 1000–1100 MPa). Such a model is most consistent with all the current inter-related geological and geochemical-isotopic data from the Kolli Massif.

To conclude, the field relations in the Kolli Massif suggest that the original iron oxide–silica-bearing sediments were deposited as chemical precipitates on a passive continental margin together with thick shelf carbonates and extensive magnetite quartzites. The Sittampundi anorthositic layered complex originally formed in the magma chamber of an island arc (Dharma Rao et al. 2013). The BIF and layered complexes were invaded by batholitic proportions of TTG melts probably in an active continental margin, and were subducted to depths as indicated by the presence of eclogites and the calculated *P-T* conditions; subsequent continental collision would have assisted conversion of the tonalitic protoliths into high-grade tonalitic orthogneisses. Exhumation and uplift of the package enabled cooling that gave rise to amphibolite-facies assemblages recorded locally in the Kolli Massif. During subduction, exhumation, and uplift the BIFs were infiltrated by fluids, most likely saline to hypersaline in nature, which effected mass transfer of various additional elements such as Mg, Al, Ca, etc., which resulted in the formation of orthopyroxene +/- clinopyroxene +/- garnet +/- amphibole as reaction textures along magnetite-quartz grain boundaries sometime during this *P–T* trajectory. This premise is further supported by a set of experiments at 800 to 900 °C and 800 to 1000 MPa, which reproduces orthopyroxene reaction textures along magnetite-quartz grain boundaries. As a side-note, it is interesting that the above lithological and tectonics relations are comparable with those in the Andean-type margins of North and South America from Alaska to Tierra del Fuego described by Lee et al. (2007), who also presciently predicted similar occurrences in the Archean.

References

Alexander BW, Bau M, Andersson P, Dulski P (2008) Continentally-derived solutes in shallow Archean sea-water: rare earth elements and Nd isotope evidence in iron formation from the 2.9 Ga Pongola Supergroup, South Africa. Geochim Cosmochim Acta 72:338–394

Anderson JR, Payne JL, Kelsey DE, Hand M, Collins AS, Santosh M (2012) High-pressure granulites at the dawn of the Proterozoic. Geology 40:431–434

Angiboust S, Harlov D (2017) Ilmenite breakdown and rutile-titanite stability in metagranitoids: natural observations and experimental results. Am Mineral 102:1696–1708

Behera BM, Waele BD, Thirukumaran V, Sundaralingam K, Narayanan S, Sivalingam B, Biswal TK (2019) Kinematics, strain pattern and geochronology of the Salem-Attur shear zone: tectonic implications for the multiple sheared Salem-Namakkal blocks of the Southern Granulite terrane, India. Precamb Res 324:32–61

Bekker A, Slack JF, Planavsky N, Krapez B, Hofmann A, Konhauser KO, Rouxel OJ (2010) Iron formation: the sedimentary product of a complex interplay among mantle, tectonic, oceanic and biospheric processes. Econ Geol 105:467–508

Bekker A, Planavsky N, Rasmussen B, Krapez B, Hofmann A, Slack J, Rouxel OJ et al (2014) Iron formations: their origins and

implications for ancient seawater chemistry. In: Holland H, Turekian K (eds) Treatise on geochemistry, vol 9. pp 561–628

Belyanin GA, Rajesh HM, Sajeev K, Van Reenen DD (2012) Ultrahigh-temperature metamorphism from an unusual corundum+orthopyroxene intergrowth bearing Al–Mg granulite from the Southern Marginal Zone, Limpopo Complex, South Africa. Contrib Mineral Petrol 164:457–475

Berman RG, Aranovich LY, Pattison DRM (1995) Reassessment of the garnet-clinopyroxene Fe-Mg exchange thermometer: II. thermodynamic analysis. Contrib Mineral Petrol 119:30–42

Bhaskar Rao YJ, Chetty TRK, Janardhan AS, Gopalan AS (1996) Sm–Nd and Rb–Sr ages and P-T history of the Archean Sittampundi and Bhavani layered meta-anorthosite complexes in Cauvery shear zone, south India - evidence for Neoproterozoic reworking of Archean crust. Contrib Mineral Petrol 125:237–250

Bhowmik SK (2006) Ultra high temperature-metamorphism and its significance in the Central Indian Tectonic Zone. Lithos 92:484–505

Bonnichsen B (1969) Metamorphic pyroxenes and amphiboles in the Biwabik Iron Formation, Dunka River area, Minnesota. Mineral Soc Am Spec Pap 2:217–241

Bradley DC (2008) Passive margins through earth history. Earth Sci Rev 91:1–26

Braun I, Kriegsman LM (2003) Proterozoic crustal evolution of southernmost India and Sri Lanka in Proterozoic East Gondwana. In: Yoshida M, Windley BF, Dasgupta S (eds) Geol Soc Lond Spec Publ 206:169–202

Brey GP, Köhler T (1990) Geothermobarometry in four-phase lherzolites II. new thermobarometers, and practical assessment of existing thermobarometers. J Petrol 31:1353–1378

Butler P (1969) Mineral compositions and equilibria in the metamorphosed iron-formation of the Gagnon region, Quebec, Canada. J Petrol 10:56–101

Chadwick B, Vasudev VN, Hegde GV (2000) The Dharwar Craton, southern India, interpreted as the result of Late Archaean oblique convergence. Precamb Res 99:91–111

Chardon D, Jayananda M, Chetty TRK, Peucat JJ (2008) Precambrian continental strain and shear zone patterns: south Indian case. J Geophys Res 113:B08402

Chetty TRK, Mohanty DP, Yellappa T (2012) Mapping of shear zones in the Western Ghats, south-western part of Dharwar craton. J Geol Soc India 79:151–154

Chowdhury P, Chakraborty S (2019) Slow cooling at higher temperatures recorded within high-*P* mafic granulites from the southern granulite terrain, India: implications for the presence and style of plate tectonics near the Archean-Proterozoic boundary. J Petrol 60:441–486

Clark C, Collins AS, Timms NE, Kinny PD, Chetty TRK, Santosh M (2009) SHRIMP U-Pb age constraints on magmatism and high-grade metamorphism in the Salem Block, southern India. Gondwana Res 16:27–36

Collins AS, Clark C, Plavsa D (2014) Peninsula India in Gondwana: The tectonothermal evolution of the southern Granulite Terrane and its Gondwanan counterparts. Gondwana Res 25:190–203

Connolly JAD (2005) Computation of phase equilibria by linear programming: a tool for geodynamic modeling and its application to subduction zone decarbonation. Earth Planet Sci Lett 236:524–541

Dey S (2013) Evolution of Archaean crust in the Dharwar Craton: the Nd isotope record. Precamb Res 227:227–246

Dharma Rao CV, Santosh M, Sajeev K, Windley BF (2013) Chromite-silicate chemistry of the Neoarchean Sittampundi Complex, southern India: implications for subduction-related arc magmatism. Precamb Res 227:259–275

Drury SA, Holt RW (1980) The tectonic framework of South India; a reconnaissance involving LANDSAT imagery. Tectonophys 65:1–15

Dutta D, Misra S, Karmakar S (2022) Deformation mechanisms and characteristics of the meta-BIFs from an early Proterozoic shear system of the Southern Granulite Terrane (SGT). India J Struct Geol 156:104534

Floran RJ, Papike JJ (1978) Mineralogy and petrology of the Gunflint Iron Formation, Minnesota-Ontario: correlation of compositional and assemblage variations at low to moderate grade. J Petrol 19:215–288

Flude S, Haschke M, Storey M (2017) Application of bench top micro-XRF to geological materials. Mineral Mag 81(4):923–948

Fonarev VI, Pilugin SM, Savko KA, Novikova MA (2006) Exsolution textures of orthopyroxene and clinopyroxene in high-grade BIF of the Voronezh Crystalline Massif: evidence of ultrahightemperature metamorphism. J Metamorph Geol 24:135–151

Frei R, Polat A (2007) Source heterogeneity for the major components of ~3.7 Ga banded iron Formations (Isua Greenstone Belt, western Greenland): tracing the nature of interacting water masses in BIF formation. Earth Planet Sci Lett 253:266–281

Frei R, Dahl PS, Duke EF, Frei KM, Hansen TR, Frandsson MM, Jenson LA (2008) Trace element and isotopic characterization of Neoarchean and Paleoproterozoic iron formations in the Black Hills (South Dakota, USA): assessment of chemical change during 2.9-1.9 Ga deposition bracketing the 2.4-2.2 Ga first rise of atmospheric oxygen. Precamb Res 162:441–474

French BM (1968) Progressive contact metamorphism of the Biwabik Iron Formation, Mesabi Range, Minnesota. Minn Geol Surv Bull 45:103

Frost BR, Frost CD (2008) On charnockites. Gondwana Res 13:30–44

Geological and Mineralogical Map of Tamil Nadu and Pondicherry (1995) Geological Survey of India: Calcutta, scale 1:500,000

George PM, Sajeev K (2015) Crustal evolution of Kolli-massif, southern India. J Indian Inst Sci 95:187–201

George PM, Sajeev K, Santosh M, Zhai M (2019) Granulite-grade garnet pyroxenite from the Kolli-massif, southern India: Implications for Archean crustal evolution. Lithos 342–343:499–512

Ghosh JG, de Wit MJ, Zartman RE (2004) Age and tectonic evolution of Neoproterozoic ductile shear zones in the Southern Granulite Terrain of India with implications for Gondwana studies. Tectonics 23:TC3006

Gireesh RV, Sekhamo K, Jayananda M (2012) Anatomy of 2.57 - 2.52 Ga granitoid plutons in the eastern Dharwar Craton, southern India: implications for magma chamber processes and crustal evolution. Episodes 35:398–413

Glorie S, de Grave J, Singh T, Payne JL, Collins AS (2014) Crustal root of the Eastern Dharwar Craton: zircon U-Pb age and Lu–Hf isotopic evolution of the East Salem Block, southeast India. Precamb Res 249:229–246

Gole MI, Klein C (1981) High-grade metamorphic Archean banded iron-formations, Western Australia: assemblages with coexisting pyroxenes ± fayalite. Am Mineral 66:87–99

Gou LL, Zhai MG, Zhang CL, George PM, Lu JS, Zhao Y, Ao WH, Hu YH, Zi JW, Zhou F (2022) Ultrahigh temperature metamorphism and isobaric cooling of Neoarchean ultramafic-mafic granulites in the southern granulite terrain, India: phase equilibrium modelling and SHRIMP zircon U-Pb dating. J Metamorph Geol. https://doi.org/10.1111/jmg.12654

Harley SL (1987) A pyroxene-bearing meta-ironstone and other pyroxene granulites from Tonagh Island, Enderby Land, Antarctica: further evidence for very high temperature (> 980 ℃) Archean regional metamorphism in the Napier Complex. J Metamorph Geol 5:341–356

Harley SL, Motoyoshi Y (2000) Al zoning in orthopyroxene in a sapphirine quartzite: evidence for > 1120 °C UHT metamorphism in the Napier Complex, Antarctica, and implications for the entropy of sapphirine. Contrib Mineral Petrol 138:293–307

Harlov DE, Newton RC (1993) Reversal of the metastable kyanite + corundum + quartz and andalusite + corundum + quartz equilibria and the enthalpy of formation of kyanite and andalusite. Am Mineral 78:594–600

Harlov DE, Milke R (2002) Stability of corundum + quartz relative to kyanite and sillimanite at high temperature and pressure. Am Mineral 87:424–432

Harlov DE, Johansson L, Van den Kerkhof A, Förster HJ (2006) The role of advective fluid flow and diffusion during localized, solid-state dehydration: Söndrum stenhuggeriet, Halmstad, SW Sweden. J Petrol 47:3–33

Harlov DE, Milke R, Gottschalk M (2008) Metastability of sillimanite relative to corundum and quartz in the kyanite stability field: competition between stable and metastable reactions. Am Mineral 93:608–617

Harlov DE, Dunkley DJ, Hansen EC, Ishwar-Kumar C, Samuel V, Hokada T (2022) Zircon as a recorder of trace element changes during high-grade metamorphism of Neoarchean lower crust, Shevaroy Block, Eastern Dharwar Craton, India. J Petrol 63:egac036

Hazarika P, Pruseth KL, Mishra B (2015) Neoarchean greenstone metamorphism in the Eastern Dharwar Craton, India: constraints from monazite U-Th-Pb total ages and PT pseudosection calculations. J Geol 123:429–461

He HL, Wang YQ, George PM, Sajeev K, Guo JH, Lai CK, Zhai MG (2021) Formation of ~2.5 Ga Sittampundi anorthosite complex in southern India: implications to lower crustal stabilization of the Dharwar Craton. Precamb Res 354:106012

Hokada T, Horie K, Satish-Kumar M, Ueno Y, Nasheeth A, Mishima K, Shiraishi K (2013) An appraisal of Archaean supracrustal sequences in Chitradurga Schist Belt, Western Dharwar Craton, southern India. Precamb Res 227:99–119

Holland HD (2006) The oxygenation of the atmosphere and oceans. Philos Trans Royal Soc Lond B Bio Sci 361:903–915

Holland TJB, Powell R (1998) An internally-consistent thermodynamic dataset for phases of petrological interest. J Metamorph Geol 16:309–344

Huang B, Kusky TM, Wang L, Deng H, Wang J, Fu D, Peng H, Ning W (2019) Age and genesis of the Neoarchean Algoma-type banded iron formations from the Dengfeng greenstone belt, southern North China Craton: geochronological, geochemical and Sm–Nd isotopic constraints. Precamb Res 333:105437

Immega IP, Klein C (1976) Mineralogy and petrology of some metamorphic Precambrian iron-formations in southwestern Montana. Am Mineral 61:1117–1144

Ishwar-Kumar C, Windley BF, Horie K, Kato T, Hokada T, Itaya T, Yagi K, Gouzu C, Sajeev K (2013) A Rodinian suture in western India: new insights on India-Madagascar correlations. Precamb Res 236:227–251

Ishwar-Kumar C, Santosh M, Wilde SA, Tsunogae T, Itaya T, Windley BF, Sajeev K (2016) Mesoproterozoic suturing of Archean crustal blocks in western peninsular India: implications for India-Madagascar correlations. Lithos 263:143–160

Jayananda M, Moyen JF, Martin H, Peucat JJ, Auvray B, Mahabaleswar B (2000) Late Archaean (2550–2520 Ma) juvenile magmatism in the Eastern Dharwar craton, southern India: constraints from geochronology, Nd–Sr isotopes and whole rock geochemistry. Precamb Res 99:225–254

Jayananda M, Chardon D, Peucat JJ, Capdevila R (2006) 2.61 Ga potassic granites and crustal reworking in the Western Dharwar Craton, southern India: tectonic, geochronologic and geochemical constraints. Precamb Res 150:1–26

Jayananada M, Peucat JJ, Chardon D, Krishna Rao B, Fanning CM, Corfu F (2013) Neoarchean greenstone volcanism and continental growth, Dharwar Craton, southern India: constraints from SIMS U-Pb zircon geochronology and Nd isotopes. Precamb Res 227:55–76

Jayananda M, Chardon D, Peucat JJ, Tushipokla FCM (2015) Paleo- to Mesoarchean TTG accretion and continental growth in the western Dharwar Craton, southern India: constraints from SHRIMP U-Pb zircon geochronology, whole-rock geochemistry and Nd–Sr isotopes. Precamb Res 268:295–322

Jayananda M, Santosh M, Aadhiseshan KR (2018) Formation of Archean (3600–2500 Ma) continental crust in the Dharwar Craton, southern India. Earth Sci Rev 181:12–42

Jayananda M, Aadhiseshan KR, Kusiak MA, Wilde SA, Sekhamo K, Guitreu M, Santosh M, Gireesh RV (2020) Multi-stage crustal growth and Neoarchean geodynamics in the Eastern Dharwar Craton, southern India. Gondwana Res 78:228–260

Jayananda M, Guitreau M, Aadhiseshan KR, Miyazaki T, Chung SL (2023) Origin of the oldest (3600–3200 Ma) cratonic core in the Western Dharwar Craton, southern India: Implications for evolving tectonics of the Archean Earth. Earth Sci Rev 236:104278

Johannes W (1973) A simplified piston-cylinder apparatus of high precision. N Jahrb Mineral Mon 7:31–351

Johannes W, Bell PM, Mao HK, Boettcher AL, Chipman DW, Hays JF, Newton RC, Seifert F (1971) An inter-laboratory comparison of piston-cylinder pressure calibration using the albite-breakdown reaction. Contrib Mineral Petrol 32:24–38

Johnson CM, Beard B, Beukes N, Klein C, O'Leary J (2003) Ancient geochemical cycling in the Earth as inferred from Fe isotope studies of banded iron formations from the Transvaal Craton. Contrib Mineral Petrol 144:523–547

Kasting JF (2013) What caused the rise of atmospheric O_2? Chem Geol 362:13–25

Kelly NM, Harley SL (2004) Orthopyroxene–corundum in Mg–Al-rich granulites from the Oygarden Islands, East Antarctica. J Petrol 45:1481–1512

Kienast JR, Ouzegane K (1987) Polymetamorphic Al, Mg-rich granulites with orthopyroxene-sillimanite and sapphirine parageneses in Archaean rocks from the Hoggar, Algeria. Geol J 22:57–79

Kihle J, Harlov DE, Frigaard O, Jamtveit B (2010) Epitaxial quartz inclusions in corundum from a sapphirine–garnet boudin, Bamble Sector, SE Norway: SiO_2–Al_2O_3 miscibility at high P-T dry granulite facies conditions. J Metamorph Geol 28:769–784

Klein C (1978) Regional metamorphism of Proterozoic iron-formation, Labrador Trough, Canada. Am Mineral 63:898–912

Klein C (1983) Diagenesis and metamorphism of Precambrian banded iron-formation. In: Trendall AF, Morris RC (eds) Iron-formation: Facts and Problems. Elsevier, Amsterdam, pp 417–469

Klein C (2005) Some Precambrian iron formations (BIFs) from around the world: their age, geologic setting, mineralogy, metamorphism, geochemistry and origin. Am Mineral 90:1473–1499

Konhauser KO, Planavsky NJ, Hardisty DS, Robbins LJ, Warchola TJ, Hgaard R, Lalonde SV, Partin A, Oonk PBH, Tsiiikos H, Lyons TW, Bekker A, Johnson CM (2017) Iron formations; a global record of Neoarchaean to Palaeoproterozoic environmental history. Earth Sci Rev 172:140–177

Lan C, Yang AY, Wang C, Zhao T (2019a) Geochemistry, U-Pb zircon geochronology and Sm-Nd isotopes of the Xincai banded iron formation in the southern margin of the North China Craton: implications on Neoarchean seawater compositions and solute sources. Precamb Res 326:240–257

Lan C, Zhao T, Chen WT, Long X (2019b) Trace elemental modification in magnetite from high-grade metamorphosed BIFs in the southern North China Craton. Ore Geol Rev 112:103019

Lancaster PJ, Dey S, Storey CD, Mitra A, Bhunia RK (2014) Contrasting crustal evolution processes in the Dharwar Craton: insights from detrital zircon U-Pb and Hf isotopes. Gondwana Res 28:1361–1372

Lee CTA, Morton DM, Kistler RW, Baird AK (2007) Petrology and tectonics of Phanerozoic continent formation: from island arcs to accretion and continental arc magmatism. Earth Planet Sci Lett 263:370–387

Lee HY, Ganguly J (1988) Equilibrium compositions of co-existing garnet and orthopyroxene: experimental determinations in the system FeO-MgO-Al_2O_3-SiO_2 and applications. J Petrol 29:93–113

Li S, Santosh M, Ganguly S, Thanooja PV, Sajeev K, Pahari A, Manikyamba C (2018) Neoarchean microblock amalgamation in southern India: evidence from the Nallamalai Suture Zone. Precamb Res 314:1–27

Lyons TW, Reinhard CT, Planavsky NJ (2014) The rise of oxygen in Earth's early ocean and atmosphere. Nature 506:307–315

Maibam B, Gerdes A, Goswami JN (2016) U-Pb and Hf isotope records in detrital and magmatic zircon from eastern and western Dharwar Craton, southern India: evidence for coeval Archaean crustal evolution. Precamb Res 275:496–512

Manikyamba C, Ganguly S, Santosh M, Saha A, Chatterjee A, Khelen AC (2015) Neoarchean arc–juvenile back-arc magmatism in eastern Dharwar Craton, India: geochemical fingerprints from the basalts of Kadiri greenstone belt. Precamb Res 258:1–23

Mloszewska AM, Haugaard R, Konhauser K (2012) Petrography and composition of iron formation from the ca. 3.8 Ga Nulliak supracrustal association (northern Labrador, Canada). Mineral Mag 76:2120

Mohan MR, Sarma DS, McNaughton NJ, Fletcher IR, Wilde SA, Siddiqui MA, Rasmussen B, Krapez B, Gregory CJ, Kamo SL (2014) SHRIMP zircon and titanite U-Pb ages, Lu-Hf isotope signatures and geochemical constraints for ~2.56 Ga granitic magmatism in Western Dharwar Craton, southern India: evidence for short-lived Neoarchean episodic crustal growth? Precamb Res 243:197–220

Mohanty DP, Chetty TRK (2014) Possible detachment zone in Precambrian rocks of Kanjamalai Hills, Cauvery Suture Zone, Southern India: implications to accretionary tectonics. J Asian Earth Sci 88:50–61

Morey GB, Papike JJ, Smith RW, Weiblen PW (1972) Observations on the contact metamorphism of the Biwabik Iron-Formation, East Mesabi District, Minnesota. Geol Soc Am Mem 135:225–264

Mukhopadhayay B, Bose MK (1994) Transitional granulite-eclogite facies metamorphism of basic supracrustal rocks in a shear zone complex in the Precambrian shield of south India. Mineral Mag 58:97–118

Noack NM, Kleinschrodt R, Kirchenbaur M, Fonseca ROC, Muenker C (2013) Lu-Hf isotope evidence for Paleoproterozoic metamorphism and deformation of Archean oceanic crust along the Dharwar Craton margin, southern India. Precamb Res 233:206–222

Ohmoto H, Watanabe Y, Yamaguchi KE, Naraoka H, Haruna M, Kakegawa T, Hayashi KI, Kato Y (2006) Chemical and biological evolution of early Earth: constraints from banded iron formations. In: Kesler SE, Ohmoto H (eds) Evolution of early Earth's atmosphere, hydrosphere and biosphere - constraints from ore deposits. Geol Soc Am 198:291–332

Peucat JJ, Jayananda M, Chardon D, Capdevila R, Fanning CM, Paquette JL (2013) The lower crust of the Dharwar Craton, southern India: patchwork of Archean granulitic domains. Precamb Res 227:4–28

Plavsa D, Collins AS, Foden JF, Kropinski L, Santosh M, Chetty TRK, Clark C (2012) Delineating crustal domains in Peninsular India: age and chemistry of orthopyroxene-bearing felsic gneisses in the Madurai Block. Precamb Res 198–199:77–93

Plavsa D, Collins AS, Payne JL, Foden JD, Clark C, Santosh M (2014) Detrital zircons in basement metasedimentary protoliths unveil the origins of southern India. Geol Soc Am Bull 126:791–811

Prasad CVRK, Subba Reddy N, Windley BF (1982) Iron formations in Archean granulite-gneiss belts with special reference to southern India. J Geol Soc India 23:112–122

Rajesh HM (2012) A geochemical perspective on charnockite magmatism in peninsular India. Geosci Front 3:773–788

Ram-Mohan M, Satyanarayanan M, Santosh M, Sylvester PJ, Tubrett M, Lam R (2013) Neoarchean supra-subduction zone arc magmatism in southern India: geochemistry, zircon U-Pb geochronology and Hf isotopes of the Sittampundi Anorthosite Complex. Gondwana Res 23:539–557

Rameshwar Rao D, Narayanana BL, Balaram V (1991a) Nature and origin of lower crustal rocks of Dhamapuri area, Tamil Nadu, southern India – a geochemical approach. Geochem J 25:57–74

Rameshwar Rao D, Charan SN, Natarajan R (1991b) P-T conditions and geothermal gradient of gneiss-enderbite rocks: Dhamapuri area, Tamil Nadu, India. J Petrol 32:539–554

Rasmussen B, Krapez B, Meier DB (2014) Replacement origin for hematite in 2.5 Ga banded iron formation: evidence for post-depositional oxidation of iron-bearing minerals. Geol Soc Am Bull 126:438–446

Rasmussen B, Zi JW, Sheppard S, Krapez B, Muhling JR (2016) Multiple episodes of hematite mineralization indicated by U-Pb dating of iron-ore deposits, Marquette Range, Michigan, USA. Geology 44:547–550

Rasmussen B, Muhling JR, Suvorova A, Krapez B (2017) Greenalite precipitation linked to the deposition of banded iron formations down slope from a late Archean carbonate platform. Precamb Res 290:49–62

Ratheesh-Kumar RT, Santosh M, Yang Q, Ishwar-Kumar C, Chen N, Sajeev K (2016) Archean tectonics and crustal evolution of the Biligiri Rangan Block, southern India. Precamb Res 275:406–428

Ratheesh-Kumar RT, Windley BF, Xiao WJ, Jia XL, Mohanty DP, Zeba-Nezrin FK (2020) Early growth of the Indian lithosphere: implications from the assembly of the Dharwar Craton and adjacent granulite blocks, southern India. Precamb Res 336:105491

Saitoh Y, Tsunogae T, Santosh M, Chetty TRK, Horie K (2011) Neoarchean high pressure metamorphism from the northern margin of the Palghat-Cauvery Suture Zone southern India. J Asian Earth Sci 42:268–285

Sajeev K, Osanai Y (2004) Ultrahigh-temperature metamorphism (1150 °C, 12 kbar) and multistage evolution of Mg-, Al-rich granulites from the Central Highland Complex, Sri Lanka. J Petrol 45:1821–1844

Sajeev K, Windley BF, Connolly JAD, Kon Y (2009) Retrogressed eclogite (20 kbar, 1020 °C) from the Neoproterozoic Palghat-Cauvery suture zone, southern India. Precamb Res 171:23–36

Samuel VO, Santosh M, Liu S, Wang W, Sajeev K (2014) Neoarchean continental growth through arc magmatism in the Nilgiri Block, southern India. Precamb Res 245:146–173

Samuel VO, Harlov DE, Kwon S, Sajeev K (2019) Silicate, oxide, and sulphide trends in neo-Archean rocks from the Nilgiri Block, southern India: the role of fluids during high-grade metamorphism. J Petrol 60:1027–1062

Sandiford M, Powell R (1986) Pyroxene exsolution in granulites from Fyfe Hills, Enderby Land, Antarctica: evidence for 1000 °C metamorphic temperatures in Archean continental crust. Am Mineral 71:946–954

Santosh M, Maruyama S, Sato K (2009) Anatomy of a Cambrian suture in Gondwana: pacific-type orogeny in southern India? Gondwana Res 16:321–341

Santosh M, Yang QY, Shaji E, Tsunogae T, Ram Mohan M, Satyanarayanan M (2015) An exotic Mesoarchean microcontinent: the Coorg Block, southern India. Gondwana Res 27:165–195

Santosh M (2020) The southern granulite terrane: a synopsis. Episodes 43:109–123

Saravanan S (1969) Origin of iron ores of Kanjamalai, Salem District, Madras state. Indian Mineral 10:236–244

Sato K, Santosh M, Tsunogae T, Chetty TRK, Hirata T (2011) Subduction-accretion collision history of the Gondwana suture in southern India: a laser ablation ICP-MS study of zircon chronology. J Asian Earth Sci 40:162–171

Satish-Kumar M, Shirakawa M, Imura A, Otsuji-Makino N, Imanaka-Nohara R, Malaviarachchi SPK, Fitzsimons ICW, Sajeev K,

Grantham GH, Windley BF, Hokada T, Takahashi T, Shimoda G, Goto KT (2021) A geochemical and isotopic perspective on tectonic setting and depositional environment of Precambrian meta-carbonate rocks in collisional orogenic belts. Gondwana Res 96:163–204

Scribano V, Carbone S (2020) Convective instability in intraplate oceanic mantle caused by amphibolite-derived garnet-pyroxenites - a xenolith perspective (Hyblean Plateau, Sicily). Geosciences 10:378

Sengupta P, Raith MM, Kooijman E, Talukdar M, Chowdhury P, Sanyal S, Mezger K, Mukhopadhay D (2015) Provenance, timing of sedimentation and metamorphism of metasedimentary rock suites from the southern granulite terrane, India. Geol Soc Lond Mem 43:297–308

Sharp ZD, O'Neil JR, Essene EJ (1988) Oxygen isotope variations in granulite-grade iron formations: constraints on oxygen diffusion and retrograde isotopic exchange. Contrib Mineral Petrol 98:490–501

Simmons EC, Lindsley DH, Papike JJ (1974) Phase relations and crystallization sequence in a contact-metamorphosed rock from the Gunflint Iron Formation, Minnesota. J Petrol 15:539–565

Sreehari L, Toyoshima T (2020) Structural architecture and geological relationships in the southern part of Chitradurga Schist Belt, Dharwar craton, south India. J Mineral Petrol Sci 115:102–117

Subramaniam AP (1956) Mineralogy and petrology of the Sittampundi Complex, Salem district, Madras State, India. Geol Soc Am Bull 67:317–390

Takahashi T, Shuto K (1997) Major and trace element analysis of silicate rocks using X-ray fluorescence spectrometer RIX3000. Rigaku-Denki J 28:25–37

Thirunavukkarasu A, Rajendran S, Suresh R, Sakthivel C, Kasilingam C, Sankar M (2015) Geochemistry of iron ore deposits of Tirthamalai area, Dharmapuri District, Tamil Nadu, India; implication on the genesis. J Appl Geochem 17:462–470

Tomson JK, Bhaskar Rao YJ, Vijaya Kumar T, Choudhary AK (2013) Geochemistry and neodymium model ages of Precambrian charnockites, Southern Granulite Terrain, India; constraints on terrain assembly. Precamb Res 227:295–315

Tushipokla JM (2013) Geochemical constraints on komatiite volcanism from Sargur Group Nagamangala greenstone belt, western Dharwar Craton, southern India: implications for Mesoarchean mantle evolution and continental growth. Geosci Front 4:321–340

Vaniman DT, Papike JJ, Labotka T (1980) Contact metamorphic effects of the Stillwater Complex, Montana; the concordant iron-formation. Am Mineral 65:1087–1102

Yang QY, Santosh M (2015) Zircon U-Pb geochronology and Lu-Hf isotopes from the Kolar greenstone belt, Dharwar craton, India: implications for crustal evolution in an ocean-trench-continental transect. J Asian Earth Sci 113:797–811

Yellappa T, Santosh M, Chetty TRK, Kwon S, Park C, Nagesh P, Mohanty DP, Venkatasivappa V (2012) A Neoarchean dismembered ophiolite complex from southern India: geochemical and geochronological constraints on its suprasubduction origin. Gondwana Res 21:246–265

Yellappa T, Chetty TRK, Santosh M (2016) Precambrian iron formations from the Cauvery Suture Zone, southern India: implications for sub-marine hydrothermal origin in Neoarchean and Neoproterozoic convergent margin settings. Precamb Res 72:1177–1196

Zhai M, Windley BF (1990) The Archaean and early Proterozoic banded iron formations of North China: their characteristics, geotectonic relations, chemistry and implications for crustal growth. Precamb Res 48:267–286

Zhai M, Windley BF, Sills JD (1990) Archaean gneisses, amphibolites and banded iron-formations from the Anshan area of Liaoning Province, NE China; their geochemistry, metamorphism and petrogenesis. Precamb Res 46:195–216